HD 129590: A Binary System with an Exocomet Belt

Sofia Slaniceanu

Division of Astrophysics
Department of Physics

Lund University

2026-EXA255 FYSK04

Degree project of 15 higher education credits
May 2026

Supervisor: Aline Novais
Co-supervisor: Jens Hoeijmakers

Division of Astrophysics
Department of Physics
Box 118
SE-221 00 Lund
Sweden

Abstract

HD 129590 is a stellar system with a directly imaged debris disk located in the Scorpius–Centaurus association, approximately 420 light years away. With an estimated age of 15 Myr, young systems like HD 129590 have been ideal for studying the development and evolution of exocomets and planetary disks at early epochs of star formation, at a time when such structures are just emerging. Consequently, previous literature has afforded attention to the system's debris disk as part of such efforts. However, in focusing on the debris disk, the internal, as well as orbital, stellar parameters remain uncertain. In this thesis, the properties of the HD 129590 system are investigated in order to shed more light on the stellar components. This is achieved through the analysis of archival high-resolution spectra taken via the High Accuracy Radial velocity Planet Searcher (HARPS) spectrograph over different time intervals. Visual inspection of the spectra illustrate that the stellar system under investigation is in fact a binary system composed of two stars. The spectra thus display the characteristics of double-lined spectroscopic binaries. To characterise the orbits of the binary stars, double Voigt profiles are fitted over a selection of lines, whose peak positions enable the extraction of the radial velocities of the stars at different epochs. Over these radial velocity measurements, Keplerian orbits are fitted, thereby extracting the orbital parameters for the two stars. The results reveal a highly eccentric system, with a period of approximately 23 days, and a median mass ratio $q = 1.001 \pm 7\%$. To characterise the internal properties of the two stars, the `pySME` software is utilised. Through the software, approximately 30 segments within a roughly 1000 Å spectral region are fit for each star in order to obtain parameters such as effective temperature, surface gravity, metallicity, and projected equatorial radial velocity. The results suggest stars on the boundary between a G-type star and an F-type star, with effective temperatures around 6400 K with uncertainties. Finally, a discussion is had with regards to the limitations of the project, as well as to future work that can be performed to better understand this system.

Popular Science Summary

Spectroscopy, the Key to the Heart of any Star

Have you ever wondered what stars are made of? How could we even tell? It's not like we can just send a spaceship to collect a sample of the Sun, bring it back to Earth, and study it under a microscope. Thankfully, even if we could, we don't need to go through all of that. Instead, we can study something which is in practically infinite abundance, and readily available to us. That something is starlight. Studying the light from a star in order to determine its properties bears the name of stellar spectroscopy.

Spectroscopy has had its emergence relatively recently. Its beginning as a modern method of scientific investigation can be traced to the scientific revolutions of the 1600s, when light was first split into constituent components by Isaac Newton in 1672. This revealed that white light is a combination of colors. This combination of colors gave birth to the "visible spectrum", a spectrum of colors emerging from the separation of visible light. Sometime later in 1814, the German Joseph von Fraunhofer discovered narrow dark streaks at seemingly irregular intervals running across the spectrum of the Sun, appropriately named "Fraunhofer lines". About half a century later, Gustav Kirchhoff and Robert Bunsen provided the explanation for those mysterious lines. By comparing them with emission lines from laboratory samples, it was revealed that these lines are caused when atoms and molecules from the atmospheres of these stars absorb light from the star, hence more generally these dark features are referred to as "absorption" features.

To the study of the stars, the observations of Kirchhoff and Bunsen were crucial. Light is absorbed at certain wavelengths thanks to the internal structure of atoms and molecules. Light, as electromagnetic radiation, can be thought of as a wave, similar to sound. Light at different wavelengths carries different energies. At the same time, atoms contain electrons in different orbitals, different orbits around the atomic nucleus. But these electrons are not fixed, they may migrate to different orbitals, provided that enough energy is put into them to make that jump. In the atmospheres of stars, such transfers of energy can occur when the light of the star intersects atoms in the stellar atmosphere, leading to the atom's absorption of the photon of light. These absorption energies and wavelengths depend, thus, on individual atoms, allowing us to identify the presence or absence of elements in a star. Furthermore, the abundance of an element can also be measured. The more abundant an element, the deeper and darker the absorption line will be, since there will be more atoms to absorb at that particular wavelength.

While normally an element would produce absorption features at certain wavelengths, different properties of the star impact the way the feature appears. For example, if a star were to be moving towards the observer, the emitted light, and therefore its spectrum, would be compressed, while if it was moving away it would be stretched, according to the Doppler effect. This translates into the absorption lines moving to lower or higher wavelengths depending on whether the star is moving towards you or away from you, respectively. Putting together all this, through spectroscopy we can analyse fundamental properties of stars, their orbital parameters such as velocities and period, as well as their internal properties such as temperature and mass.

In this project, I look at multiple high-resolution spectra collected with the HARPS spectrograph for the HD 129590 system. This is a young stellar system, relatively close by, with an imaged protoplanetary disk, which is all the gas, dust, and debris left over from the formation of the stellar system, and which then is in gravitational orbit around the system. From such a disk, it could be that one day planets, perhaps like the Earth, will form, or have already just formed. But to know if this fascinating scenario is worth entertaining, we must investigate first the properties of the system. To that end, I first look at the spectra to confirm the binary nature of the system, where HD 129590 is a pair of stars, embraced in a gravitational dance. As they dance around in their orbits opposite of each other, the Doppler effect splits every spectral line in two, enabling the identification of the binary. This line splitting further enables the calculation of the radial velocities of the two stars from the wavelength shift, which I use to characterise the orbital system of the binary stars. Lastly, I fit synthetic spectra of model stars over the observed spectra to see which models match best with the data, enabling me to determine the effective temperatures, metallicities and elemental abundances of my two stars.

In the long run, describing the properties of the stars in the system will enable deeper study of the system as a whole, with its protoplanetary disk, and how such disks may evolve under the influence of their stars. Crucially, since planets are thought to emerge from such disks, young systems like HD 129590 are ideal. Their age enables astronomers to study systems at ages at which planets are thought to first develop, bridging a gap not just in general knowledge, but in the knowledge of our own system. Understanding such young systems can offer clues as to the Solar System's own evolution, and perhaps to the birth of our own planet Earth, and the subsequent emergence of life therein.

Acknowledgements

I would like to extend my deepest gratitude to my supervisor, Aline Novais, and my co-supervisor, Jens Hoeijmakers, for allowing me the opportunity to partake in this project, and for guiding me along the way with their invaluable words of advice. Additional due thanks to Adrien Simonnin, who offered to read and provide useful feedback on this thesis. I would also like to thank Brian Thorsbro, for all the crucial aid particularly in the latter half of the project with the ever-capricious `pySME` wrapper, as well as for providing me with the Gaia-ESO element linelist. Due thanks is also directed to the numerous astronomers that compiled the linelist and continue to keep it updated. In addition, I would like to extend further appreciation to the entire exoplanet research group.

Exceptional credit must also go to my parents and to my family, whose support of my journey in Sweden made all of this possible. To my friends too, for having made my Swedish adventure much more than just an academic journey, and endowed me with enough memories to last a lifetime.

Last but not least, I am eternally grateful to my partner, Aira, for her continuous support throughout this exciting, yet not without its perils, period. You were the anchor to my ship in troubled times, and a ray of light more potent than the Sun in more auspicious days.

Contents

1 Introduction

Over the last couple of decades, improvements in various techniques and instrumentation have enabled astronomers to detect and study exocomets and protoplanetary environments around stars other than the Sun. Through the study of such environments at different stages in the lifetime of stars, insights can be gained about their evolution over time. These insights in turn enable a more thorough understanding of how such structures could develop into more mature planetary systems, and how different characteristics of the host stars alter that development. One essential foundational step in such studies is the characterisation of the stellar system within which the protoplanetary component is found. In this work, the object under investigation is HD 129590, a relatively young stellar system with a directly imaged debris disk.

The Scorpius-Centaurus OB association is the nearest and most well studied representative of OB associations (e.g. Blaauw, 1946, Fang and Herczeg, 2025). Such associations represent gravitationally unbound stellar densities dominated in terms of luminosities by O- and B-type member stars, although containing a variety of less prominent stellar types (Wright, 2020). HD 129590 is such a fainter member of the Scorpius-Centaurus complex, situated within the Upper Centaurus Lupus subgroup, at a distance of roughly 135 parsec, or 420 light years (Chen et al., 2011, system referred to as HIP 72070). The estimated age of the subgroup and its members is of roughly 15 Myr (Mamajek et al., 2002). Additionally, this system is observed to posses a debris disk, which was directly imaged (e.g. Matthews et al., 2017, Olofsson et al., 2023). Consequently, this relatively nearby system has been an attractive target of observation for the study of the evolution of young debris disks. And yet despite this attractiveness, the properties of the stellar system itself have not been thoroughly determined, and while there are indications that the system might be a binary (Grandjean et al., 2023), the system is largely listed in literature as a single Sun-like star (e.g. Kral et al., 2020, Olofsson et al., 2023). So far, it seems that the scientific attention accorded to this system has been focused on studying its debris disk. Consequently, and in particular for direct imaging of the disk, the stellar system has usually been masked with a choronograph (as described, for instance, in Matthews et al., 2017). Characterisation of the stellar system itself appears to have only been conducted as part of photometric surveys (e.g. Chen et al., 2011), with limited numbers of observations. However, particularly when analysing the dynamical evolution of the debris disk and its properties, accurately characterising the host stellar properties becomes crucial. A more focused spectroscopic analysis of the stellar system for the purpose of confirming or re-evaluating its dynamical and internal properties makes itself thus necessary.

In this project, the stellar system HD 129590 is analysed in an effort to determine some of its stellar parameters in greater detail than expounded by present literature. This is done via analysis performed on archival spectra collected with the High Accuracy Radial velocity Planet Searcher (HARPS) spectrograph over different observational epochs spanning a time interval between 2019 to 2020. Initial visual inspection of the spectra reveals dynamic and periodic spectral features characteristic of double-lined spectroscopic binaries. Absorption lines in these spectra thus appear doubled as a consequence of the spectral contributions of both stars, Doppler shifted in accordance with the orbital motions of the stars along the center of mass of the system. Initially, therefore, Voigt profiles are fit to six selected spectral lines in order to extract the two stars' radial velocities over the available epochs, and to thereby calculate the weighted average of those radial velocities. This enables the fitting of Keplerian profiles to the subsequent curve of radial velocity over time in order to characterize the binary orbit with its orbital parameters like period P and eccentricity e. Then, a wide region of the spectrum at a given epoch is taken and fitted with the `pySME` software (Wehrhahn et al., 2023). For the fitting procedure, 32 segments within the wide region are utilised, covering around 7000 observation pixels within the `sme` structure. Such wide spectral pixel coverage and numerous line selection is deemed necessary for the accurate extraction of internal stellar parameters for the two stars, parameters such as effective temperature (T_{eff}), surface gravity ($\log g$), projected equatorial radial velocity ($v \sin i$), as well as the stellar metallicities. In the concluding section, a discussion will be developed with regards to the limitations of the dataset, and suggested improvements for future research. In addition, comments will be given with regards to new potential research pertaining the HD 129590 system, in particular to the idea of N-body simulations that could help characterise the dynamics of the observed debris disk.

2 Theoretical Framework

2.1 Spectral Classification of Stars

The spectra of stars manifest primarily in the form of absorption spectral features. As electromagnetic radiation in the form of photons travels through the stellar atmosphere, atoms and ions present therein may absorb such radiation with energies corresponding to the energies between two quantum states of those atoms and ions. In the presence of many atoms and ions of a given type, many such absorptions may occur, resulting in a decrease in measured flux at the wavelength corresponding to the transition energy between the two quantum states (Karttunen et al., 2017). An example of a spectrum of the target stellar system, HD 129590, is illustrated in Figure 1.

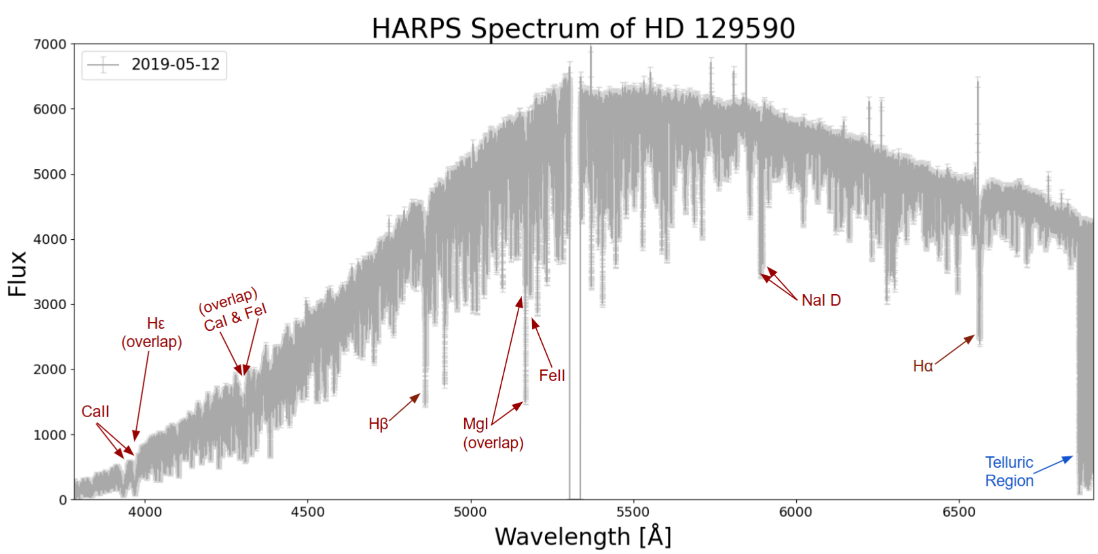

Figure 1: Example spectrum of HD 129590 acquired with the HARPS spectrograph in 2019-05-12, program ID 0103.C-0206(A), PI De Medeiros. Some prominent lines have been labeled. Note the region of prominent telluric absorption, caused by absorptions within Earth's atmosphere.

Different stellar properties, such as temperature, pressure, and surface gravity, affect the way the spectrum of a star may look in various ways. For instance, the temperature at the surface of a star determines the occupancy ratios of different excited levels with respect to the ground state within the population of an atom, according to the Boltzmann distribution:

$$\frac{N_{\text{upper}}}{N_{\text{lower}}} \propto e^{-kT}, \tag{1}$$

where N_{upper} is the atomic population in an upper state, N_{lower} is the population in a lower quantum state, k is the Boltzmann constant, and T is the atomic excitation temperature. As such, different stellar temperatures will enable different atomic transitions, and hence different observed absorption spectral lines.

Considering such differences, it becomes convenient to classify stellar populations in different groups. One common system of stellar classification is the Harvard classification, originally compiled by Annie Jump Cannon and published in the form of the Henry Draper catalogue (Cannon and Pickering, 1918), which was based primarily on the visual inspection of stellar spectra and their classification based on temperature and luminosity. From hottest to coolest types, the Harvard spectral classification proceeds as:

O - B - A - F - G - K - M.

A further subdivision of each stellar type exists in the form of numbers, ranging from 0 to 9, usually integer increments of 1, but with decimals possible, where 0 corresponds to the hottest stars of the type, and 9 to the coolest. Additionally, for a luminosity description, the Yerkes classification is also in wide use, manifesting in the form of Roman numerals from I to V, where I represents the most luminous, or *supergiants*, and V represents the least luminous stars, or *dwarfs*. Thus, the spectral classification of the Sun is G2V, a relatively cool dwarf star, but which is relatively hot for its G-type (e.g. Apellániz et al., 2024).

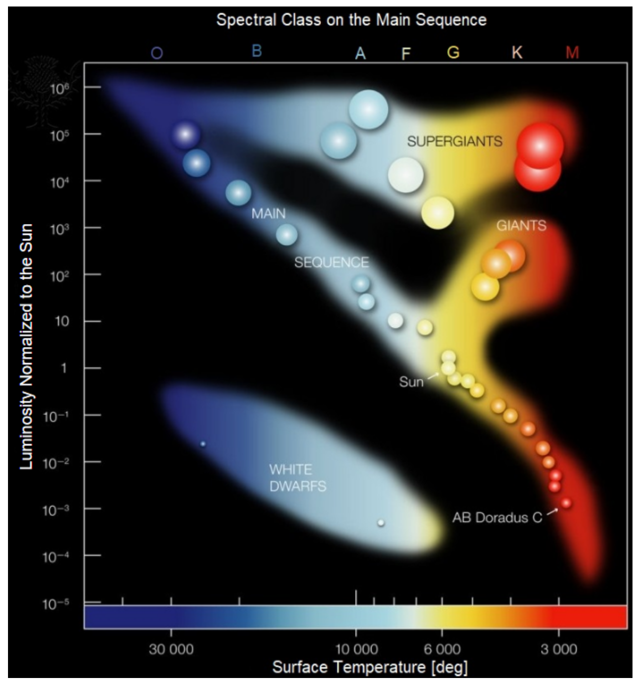

Figure 2: Illustrative Hertzsprung-Russell diagram showing the distribution of stars as surface temperature vs. stellar luminosity relative to the Sun. The approximate ranges of the stellar spectral classes have been added. Some stars are labeled for reference. Different colors show the visual appearance of the different types of stars. Image adapted from the European Southern Observatory under a CC BY 4.0 license [1].

[1]https://www.eso.org/public/unitedkingdom/images/eso0728c/?lang

A useful visual tool in understanding the correlation between different spectral classes and their properties has been the Hertzsprung-Russell diagram, one such version being illustrated in Figure 2, which plots the distribution of stars as luminosity vs. temperature. The stellar luminosity is a measure of the emitted power of the star, and scales as:

$$L \propto R^2 T_{\text{eff}}^4, \tag{2}$$

where R is the stellar radius, and T_{eff} is the effective temperature. In effect, the larger and hotter the star, the more luminous it is.

In addition, the HR diagram reveals that stars are normally clustered along select regions, which are linked to various stages in the lives of stars and linked to the internal nuclear processes which fuel stellar burning. On the main sequence lie stars which have not exhausted their primary nuclear fuel. The giant branches are populated by stars nearing the ends of their nuclear fuel, and where stars begin to expand and shed their outer layers as hydrostatic equilibrium is lost. The subsequent final fate of a star once it leaves the main sequence is then heavily dependent on its initial mass. The least massive stars, up to $8M_\odot$ end up as white dwarfs, exemplified in the bottom left of the diagram in Figure 2.

2.1.1 Young Stars and Debris Disks

Young stellar systems, such as the target of this project, HD 129590, as they form out of the initial molecular cloud, commonly exhibit so-called debris disks. These are minor objects ranging from micrometer-sized dust grains to extrasolar comets, asteroids, and dwarf planets (e.g. Pearce, 2026, Stein et al., 2026). They may be sustained through destructive processes, such as collisions between minor bodies, or the sublimation of infalling extrasolar comets. Different techniques have been developed to detect such disks. In the case of the target system HD 129590 its debris disk has been directly imaged in scattered-light observations, where the observed photons are scattered by the dust in the debris disk (Matthews et al., 2017). This disk was then subsequently the subject of scientific investigation (e.g. Kral et al., 2020, Grandjean et al., 2023), and while such an investigation is not carried out in this project, it is worth noting its existence, particularly with regards to its potential consideration in future projects (see Conclusion and Future Work).

2.1.2 Doppler Shifts of Spectral Lines

Stars themselves are objects in motion, whether they orbit around their host galaxies or a common center of mass within their own systems. From the point of view of an outside observer, the velocity at which an observed star moves may be deconstructed into two components, one tangential to the line of sight called tangential velocity v_t, and another component along the line of sight named radial velocity v_r. This radial component indicates whether the star is moving towards the observer, or away from the observer, resulting in the so-called *blueshift* or *redshift*, respectively. This motion induces a Doppler effect by causing the electromagnetic radiation from the star to either stretch or compress. This manifests in the spectrum of a star, shifting the wavelength of a spectral feature away from the rest (or laboratory) wavelength according to:

$$\frac{\lambda_{\text{obs}} - \lambda_{\text{lab}}}{\lambda_{\text{lab}}} = \frac{v_r}{c}, \tag{3}$$

where λ_{obs} is the observed wavelength of a spectral line, λ_{lab} is the laboratory wavelength of that same line, v_r is the radial velocity of the star, and c is the speed of light. Consequently, for a blueshift, λ_{obs} is smaller than λ_{lab}, i.e. to the blue of the spectrum, resulting in a negative radial velocity, while for a redshift, λ_{obs} is greater than λ_{lab}, i.e. shifted further to the red of the spectrum, resulting in a positive radial velocity.

In so-called double-lined spectroscopic binary star systems, each star possesses a radial velocity as it orbits opposite of the other in an orbit around the system's common center of mass. As such, at one epoch one star would exhibit blueshifted lines relative to the observer, while the other would be redshifted. These contributions from both stars manifest in the combined spectrum of the stellar system, leading to doubled features in said spectrum, where one feature is blueshifted, while the other is redshifted, in accordance with the movements of the stars.

2.1.3 Line Broadening

Spectral features are not infinitely narrow and sharp. A number of quantum mechanical effects give rise to broadenings of spectral lines, and the shape of spectral lines are known as line profiles. The natural width of a spectral line γ arises from Heisenberg's uncertainty principle,

$$\Delta E \Delta t \approx \hbar,$$

and is defined as:

$$\gamma = \frac{\Delta E_i + \Delta E_f}{\hbar}, \tag{4}$$

where ΔE represents the energy uncertainty arising from the uncertainty principle, and $\hbar$ is the reduced Planck constant. The subscripts i and f denote the initial and final transition states of an atom respectively, for the corresponding spectral feature (Karttunen et al., 2017).

In addition, there is Doppler broadening, which arises as a consequence of the Doppler effect applied to individual atoms. Atoms in the stellar atmosphere move in different directions and at different velocities, depending on the temperature of the layer they are at. As such, the absorption lines arising from individual atoms are undergoing a slight Doppler shift which, overall, leads to the Doppler broadening of a spectral feature. Collisional broadening is another effect which induces a widening of the spectral lines. This arises within a high pressure gas as atoms collide, increasing the uncertainty in energy. This effect may be described by a Lorentz profile (Rybicki and Lightman, 1979). More generally, a convolution of Doppler and Lorentzian broadening is described by a so-called Voigt profile. However, the implementation of the Voigt convolution function was found to be challenging. Consequently, for this project, the pseudo-Voigt approximation is used (e.g. Ida et al., 2000), which instead of a proper convolution, treats the Voigt function as a linear combination of the Gaussian and Lorentzian profiles.

For this project, different Gaussian, Lorentzian and Voigt profiles are fit and compared to spectral features in order to extract stellar properties such as radial velocity measurements (see Method). Accordingly, the Gaussian, Lorentzian, and Voigt profiles are computationally expressed as:

$$\text{Gauss}(a, v_r, \sigma, v) = a \cdot \exp\left(-\frac{(v - v_r)^2}{2\sigma^2}\right), \tag{5}$$

for the Gaussian profile, where a represents the profile amplitude (equivalently line depth), v_r is the radial velocity position of the peak, σ is the standard deviation, and v is the radial velocity range over which the fitting is ran. For a Lorentzian, the computation is carried out as:

$$\text{Lorentz}(a, v_r, \gamma, v) = a \cdot \frac{\gamma}{(v - v_r)^2 + \gamma^2}, \tag{6}$$

where a, v_r, and v have the same interpretation as Equation (5), and γ represents the half-width at half-maximum, or the width parameter equivalent to the Gaussian case. Finally, a linear combination of these profiles may be utilised into a pseudo-Voigt profile, which is expressed as:

$$\text{Voigt}(a, \eta) = a\left(\eta \cdot \text{Lorentz} + (1 - \eta) \cdot \text{Gauss}\right), \tag{7}$$

where a retains the same interpretation, and η is a mixing ratio between the Gaussian and the Lorentzian profiles, expressed as a percentage. Physically, the Voigt profile combines the broadening effects of both a Gaussian and a Lorentzian profile, and thus being able to more accurately reproduce the shapes of spectral lines.

2.2 Orbital Mechanics

The movements of celestial objects can be empirically described by Kepler's laws, while the forces which induce that motion can be described by Newton's law of gravitation. In a system with massive bodies, these bodies will exert a gravitational pull on the others. For a system of two objects, the force may be expressed as:

$$F = G\frac{m_1 m_2}{r^2}, \tag{8}$$

where G is the gravitational constant, m_1 and m_2 are the masses of the first and second object respectively, and r is the distance between them. From this force, the Keplerian laws of motion may be derived. Originally enunciated for the objects of the Solar System, the Kepler's laws are:

1. The orbits of planets are ellipses, with the Sun at one focus.
2. The orbits of planets sweep out equal areas in equal time intervals.
3. The square of the orbital period is proportional to the cube of the semi-major axis.

The main orbital elements are illustrated in Figure 3. Thus, a is the semi-major axis, and b is the semi-minor axis. The eccentricity e, not specifically illustrated in the figure, describes the shape of the orbit, where $e = 0$ corresponds to a circular orbit, $0 < e < 1$ corresponds to an elliptical orbit, and $e \geq 1$ corresponding to a gravitationally-unbound trajectory. The inclination i gives the angular tilt of the orbit with respect to some reference plane, usually the plane of the observer. The ascending node ☊ represents the point of intersection between the plane of reference and the orbital plane, through which the celestial body ascends above the reference plane. Opposite of it there is the descending node ☋, not illustrated, through which the celestial body descends below the reference plane. Longitude of the ascending node Ω gives the angle between the reference direction and the ascending node.

The argument of periapsis ω describes the angular distance between the ascending node and the periapsis, the latter of which describes the closest approach of the celestial object relative to the primary object which it orbits. When the primary object is a star, periastron may be used instead. Finally, the true anomaly ν represents the angle between the periapsis and the position of the celestial body at a given epoch (Karttunen et al., 2017).

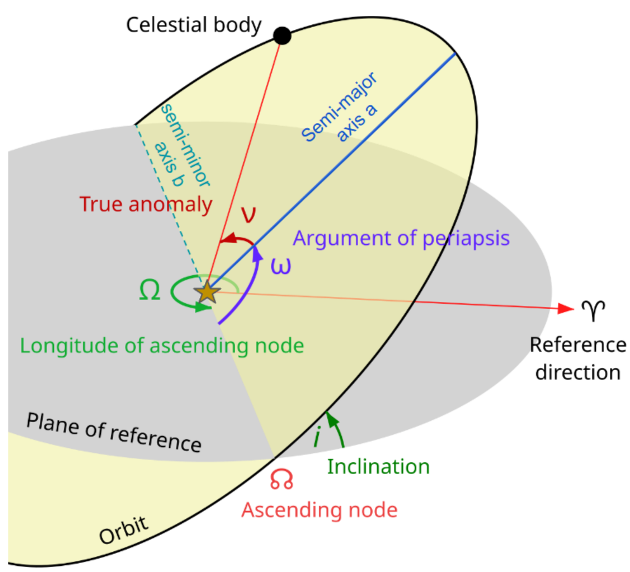

Figure 3: Illustration of the main Keplerian orbital elements, with one star pictured at the center, and an orbiting celestial body. Not illustrated here is the eccentricity. Image adapted from Wikimedia Commons, CC 3.0 license [2].

Taking these notations into account, Kepler's third law may be then expressed as:

$$4\pi^2 a^3 = G(m_1 + m_2)P^2, \tag{9}$$

where indeed a is the semi-major axis, and P is the period of the orbit.

To determine the orbital position at a given time, it is necessary to relate the observed radial velocity measurements over time with the orbital elements that describe the orbit. The radial velocity as a function of time is connected to 6 of the orbital parameters:

$$v_{\mathrm{r}}(t) = K(\cos(\omega + \nu) + e\cos\omega) + \gamma, \tag{10}$$

where K is the semi-amplitude, γ is the systemic velocity, i.e. the velocity of the entire system with regards to the observer, and ω, ν, and e are the previously defined argument of periapsis, true anomaly, and eccentricity respectively.

An intermediate step before Equation (10) can be modeled is the calculation of the true anomaly, which takes the form of:

$$\nu = 2 \cdot \arctan\left(\sqrt{\frac{1+e}{1-e}}\tan\left(\frac{E}{2}\right)\right), \tag{11}$$

where e is the eccentricity and E is the eccentric anomaly, which represents the angular distance of the celestial body on a projected auxiliary ellipse. The calculation of the true anomaly ν then takes the form of an iterative process. The Kepler equation is solved:

$$E - e\sin E = M, \tag{12}$$

where now appears the mean anomaly M, i.e. the angle which the celestial object would sweep out from the periapsis if its orbit were circular. The mean anomaly represents the initial guess based

[2] https://commons.wikimedia.org/wiki/File:Orbit1.svg

on parameters related to data, in mathematical form:

$$M = \frac{2\pi}{P}(t - t_0), \tag{13}$$

where P is the orbital period, t is the given time at which the position is calculated, and t_0 is the reference time.

Relating the radial velocity measurements with the orbital positions of stars then in principle takes the form of an iterative process. First, the mean anomaly is guessed based on variables more readily obtained from data, such as the observation time, and period. That in turn serves as the initial guess for solving the Kepler equation, which relates the mean and eccentric anomalies, derives values for the latter. That, then, gives the true anomaly, at which point the radial velocity curve can at last be modeled based on Equation (10).

2.3 Bayesian Statistics

Bayesian statistics were first developed by the British mathematician Thomas Bayes in 1763 (Bayes, 1763) as a means of improving belief or knowledge by combining an initial estimation with new data (Ivezić et al., 2014). Probability statements then grow to include, besides data, models and the parameters that describe such models. In this project, the fitting of Voigt profiles, and subsequently of radial velocity curves, all make use of Bayesian statistics to extract in particular the parameters of the Voigt, and radial velocity, models. Mathematically, the framework for Bayesian statistics is:

$$p(M, \boldsymbol{\theta}|D, I) = \frac{p(D|M, \boldsymbol{\theta}, I)p(M, \boldsymbol{\theta}|I)}{p(D|I)}, \tag{14}$$

where $p(M, \boldsymbol{\theta}|D, I)$ is called the posterior probability density function for the model M and constituent set of variables $\boldsymbol{\theta}$, given a dataset D and prior information I; $p(D|M, \boldsymbol{\theta}, I)$ is the likelihood function, i.e. the likelihood of observing the data D given the model M, with some model parameters $\boldsymbol{\theta}$, and prior information I; $p(M, \boldsymbol{\theta}|I)$ is usually called the prior, and computes the joint probability for the model and its parameters, while $p(D|I)$ is the probability of data, the evidence for the model (e.g. Ivezić et al., 2014, Barragán et al., 2019).

The priors contain information or beliefs about a given parameter, such as a range of possible values within which the true value of the parameter is expected to lie. For instance, in the case of fitting Voigt profiles to stellar lines, it can be inferred from the visual inspection of the flux vs. radial velocity plot that the profile must have a width contained within a certain range, or a depth within another range, and so on. Different kinds of priors exist depending on the amount and type of information they contain. Most used in this project are weakly or uninformative priors, which relay only that a given parameter must be situated within a certain range. Uniform priors additionally assign equal probability to all values within the given range, while within so-called Gaussian priors, a higher weight is given to an expected value, restraining the range around it within the Gaussian uncertainty σ_g. This can be due to, for instance, past measurements indicating a likely true value (Ivezić et al., 2014, Barragán et al., 2019).

2.3.1 Markov Chain Monte Carlo Algorithms

Equation (14) may be solved for the posterior distribution in various ways, but in this project the posteriors are generated from numerical sampling of parameters via Markov Chain Monte Carlo algorithms, or MCMC. Markov chains are sequences of variables where a given value depends only on the value immediately preceding it (Ivezić et al., 2014). These variables can be the parameters contained in $\boldsymbol{\theta}$, where sets of different θ_i's are generated based on, for instance, an initial θ_1 via Markov chains (Barragán et al., 2019).

In this way, starting from some θ_i, a set of models can be generated, which are then compared with data through Equation (14), obtaining posterior distributions of model parameters. These can then be the more robust constituent orbital parameters within, for instance, the fitting of the radial velocity curve to the radial velocity data. There are a number of different MCMC algorithms, but for the purpose of this project the algorithm within `numpyro.infer`[3] is used (Phan et al., 2019, Bingham et al., 2019). Throughout this project, the algorithms are initialized with 1000 warmups and 4000 samples. The warmups correspond to iterations used to tune the algorithm to the model and data and its results are not saved for posterior distributions. The subsequent samples are the iterations that are saved and contribute to the posterior distribution. The convergence of solutions can be visually inferred directly from the posterior distributions, which in the ideal case would display single density distributions centered around the most statistically relevant value for each parameter.

3 Method

3.1 Data

The dataset consists of 39 archival spectra collected with the High Accuracy Radial velocity Planet Searcher (HARPS) spectrograph at the ESO La Silla observatory (for more detailed technical descriptions of the instrument, see Pepe et al., 2000, or the ESO website[4]). These spectra were subsequently corrected for telluric absorption lines as detailed in Smette et al. (2015) prior to analysis. The dataset covers a time period ranging from 04 Feb 2019 to 12 Mar 2020, belonging to 5 observational programmes as illustrated in Table 1.

Programme ID	Principal Investigator	Epochs	Number of Spectra
0102.C-0584(A)	De Medeiros	2019 Feb 04	1
098.C-0739(A)	Lagrange	2019 Feb 13 - 2019 Apr 30	8
0103.C-0206(A)	De Medeiros	2019 May 11- 2019 Jul 20	18
1101.C-0557(D)	Lagrange	2020 Feb 27 - 2020 Mar 01	10
0104.C-0418(C)	Lagrange	2020 Mar 12	2

Table 1: Table illustrating the observational programmes from which the data is drawn, alongside the epochs they cover.

[3]https://num.pyro.ai/en/stable/

[4]https://www.eso.org/sci/facilities/lasilla/instruments/harps/inst/description.html

To note, the spectra are not collected over consecutive days, but rather irregularly, and sometimes multiple datasets are recorded over the same day, as is the case of 0104.C-0418(C). Since this is archival data, it is possible that the reason behind this observation schedule was that periodic observations were not deemed crucial to the respective scientific goals for which the data was used. With these datasets it is attempted to ascertain whether or not the system HD 129590 is a binary star system, something which is suspected in Grandjean et al. (2023), but not confirmed. In recent literature, the system continues to be referenced as a single star (e.g. Olofsson et al., 2024). In addition, through analyses of these spectra, the stellar properties will be investigated and compared with Chen et al. (2011), as well as find the radial velocities within the system, the corresponding Keplerian orbits, and the systemic velocity.

3.1.1 Flux Normalization

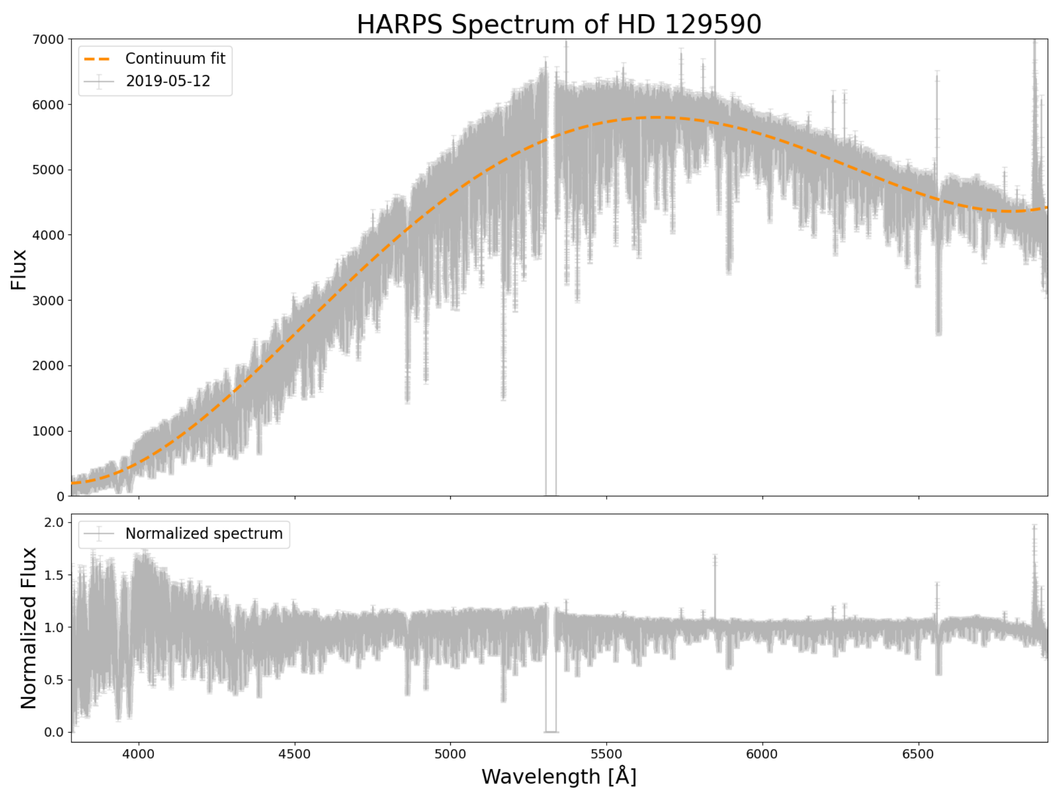

Figure 4: Top panel: a telluric-corrected spectrum of HD 129590, plotted alongside its fitted continuum, which is coloured in orange. Bottom panel: the resulting normalized spectrum obtained through the division of the spectrum by its fitted continuum for the same epoch.

Initially, the flux corresponding to each spectrum is normalized. This normalization is achieved by dividing the flux with a corresponding continuum array that matches the shape of the spectrum. The continuum array is obtained for each spectrum through the `fit_generic_continuum` function within the `specutils.fitting`[5] package (see also Earl et al., 2026). The function takes as input

[5]https://specutils.readthedocs.io/en/stable/

a spectrum and then makes use of a median filter to smooth out noise. The default polynomial model of the function is a so-called Chebyshev polynomial of degree 3, however for the purpose of this thesis that model is replaced with a generic polynomial of degree 5. The result of the division is a comparatively flat spectrum centered around unity. An example of the continuum fit, and the subsequent normalization, is illustrated in Figure 4. In particular within the middle section of the spectra, the fits seem to underappreciate the continuum value. However, the general shape is maintained, and the fits appear to recover towards regions of higher wavelength, which are the regions from which lines will be used in the fitting procedures.

This procedure is necessary for the eventual fitting with `pySME`, whose fitting structure assumes a normalized continuum. Additionally, a normalized spectrum eases the fitting of line profiles and enables clearer comparison between them. For instance, parameters such as line depth are defined relative to the continuum, and so a flat, normalized continuum enables direct comparison between line depths of various lines and for different epochs. This would be much more cumbersome to do for a continuum with a more complex shape, as then the value of the continuum would also shift.

3.2 Spectral Analysis

3.2.1 Identification as a Binary System

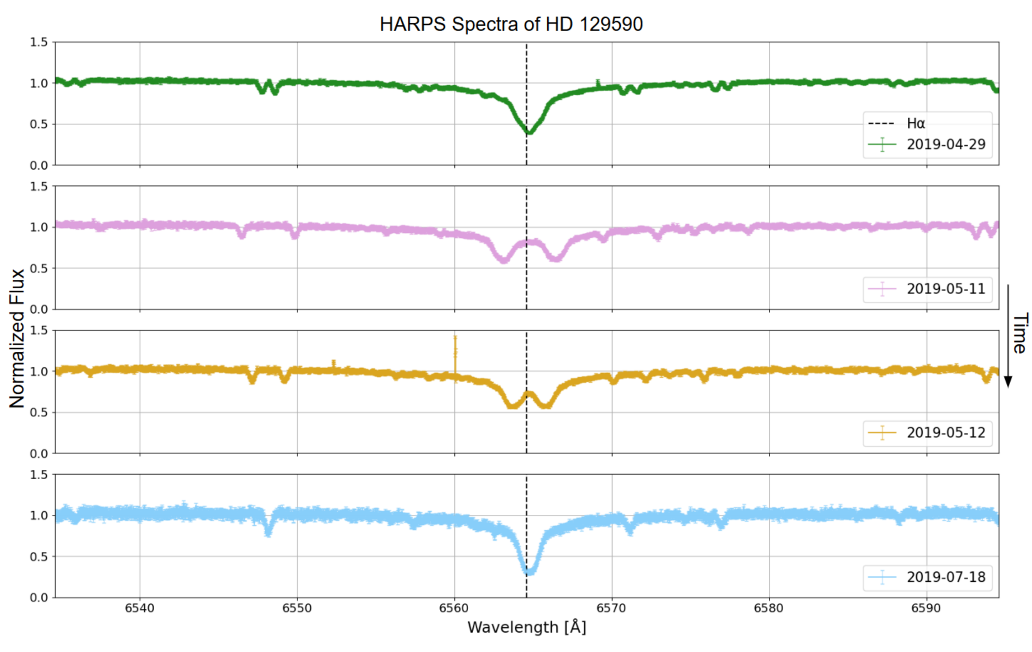

Figure 5: Different HARPS spectra of HD 129590 at progressively later epochs, in a region around the Hα line, indicated with a dashed black vertical line. The variability of the lines, their doubling and subsequent merging is visible.

The initial identification as a binary is achieved through the visual inspection of the spectra. It is observed that spectral lines appear doubled and dynamic, shifting for different epochs at different Doppler shifts, which is interpreted as reflecting the dynamical orbits of both stars along their system's common center of mass. At different epochs, a spectral line shifts in accordance with how the star producing it is moving relative to the observer. In a binary therefore, as stars move opposite of each other, spectral lines are observed at opposite Doppler shifts, producing the observed duplication. When one star fully or partially eclipses the other relative to the observer, the lines lie at the same Doppler shift, recovering a spectrum wherein every feature is a singular blended contribution from both stars. The process is illustrated in Figure 5, where a section of the spectrum in a region around the Hα is shown for different epochs. The Hα line in vacuum at $\lambda_{\mathrm{H}\alpha} = 6564.61$ Å is chosen for its broad and deep nature, and consequently relatively easier visual identification.

3.2.2 Radial Velocity Conversion

In order to obtain accurate radial velocity measurements, the wavelengths of the spectra are corrected for barycentric Earth radial velocities (BERV). These radial velocities arise from the various motions of the Earth, most notably the orbital motion around the Sun, as well as the rotational motion around its own axis (Burt et al., 2025). The correction is implemented as:

$$\lambda_{\text{corrected}} = \lambda_{\text{observed}} \cdot \left(1 + \frac{\text{BERV}}{c}\right), \tag{15}$$

where c is the speed of light, BERV is the barycentric Earth radial velocity, and $\lambda_{\text{observed}}$ is the uncorrected, observed wavelength. The values of the BERVs for each spectrum are extracted from the metadata contained within the header of each datafile associated with a respective spectrum.

The corrected wavelengths may then be converted into radial velocities via equation (3), where λ_{lab} takes the value the rest wavelength of the element which causes the absorption feature that is used for the fitting. One then obtains a spectrum with the 0th value of the x-axis at the wavelength corresponding to the λ_{lab} of a chosen line, with negative values to the left of it, and with positive values to the right of it. Extracting the peak positions on the x-axis of the spectral features then enables the measurement of the radial velocities of the stellar objects responsible for those particular spectral features.

3.2.3 Line Fitting

The fitting of spectral lines with Voigt profiles is done in order to extract radial velocity measurements for the stars at different epochs. This is achieved through `JAX`, a library for array-oriented computations similar to `numPy`, but with GPU support and accelerated differentiation, permitting running larger probabilistic analyses much faster than with `numPy` (Bradbury et al., 2018). Fitting is attempted for a variety of lines, presented in Table 2.

Certain lines, such as the Na I doublet, and the H-β, were discarded, despite being relatively more intense than many of the presented Fe I lines. In particular, the Na I doublet featured a narrow and sharp absorption line blended with the actual doublet. This sharp feature did not exhibit the same variation in wavelength attributed with a feature undergoing Doppler shift as part of stellar movement, and was thus attributed to the interstellar medium. Since that complicated the fitting process substantially, it was discarded. The Hβ line was discarded due to being surrounded by relatively strong noise and many absorption features, making the fitting, and especially the continuum parameter, very uncertain.

Thus, the main criterion behind the selection of the particular lines was their relatively flat immediate surrounding, which made the fitting function less likely to confuse the feature with another. The elements themselves which give the chosen features are not relevant to the fitting procedure, only their depth relative to their immediate surrounding.

Line	λ_{vacuum} [Å]
Fe I	5885.447
Fe I	6057.681
Fe I	6067.161
Fe I	6548.047
Hα	6564.614
Fe I	6679.828

Table 2: Table of lines selected for the fitting process to obtain radial velocity measurements, with the values of their vacuum wavelengths. The values were extracted from the NIST database (Kramida et al., 2023).

For each spectral epoch, the peak positions of the line centers are measured for each of the lines in Table 2 and saved. Since the Doppler shift is caused by stellar motion, the lines originating in that star should be equally affected, and therefore it is expected that all lines would give approximately the same radial velocity measurement. The radial velocity of one stellar component for one particular epoch will be determined through the weighted average of the radial velocities extracted from each mentioned line, in an attempt to reduce the calculated uncertainties. This weight will be calculated based on the mean uncertainty of each measurement.

For the purpose of testing the python implementations of Equations (5), (6), and (7), and to benchmark with the fitting procedures for the other lines, initially the fitting is performed for the Hα line, judged to be relatively easy to fit due to its broad and deep nature. To note, however, that a consequence of the broadness of the Hα line is that the double features will blend into one much more rapidly than the comparatively thinner Fe I features. This means that at lower absolute radial velocity values, the Hα line cannot be properly used to measure those radial velocities, as the feature will have a singular character. In such cases, the weaker lines that remain unblended are the main contribution to the radial velocity measurements. In the cases where all the utilised lines are blended, no reliable measurements could be determined, nor could such blended features be utilised in the attempted ulterior classification of features based on the particular stellar system component, i.e. on whether they belong to star 1 or star 2. In order to obtain a statistically robust fit, the best parameters are obtained via MCMC fitting for the Gaussian, Lorentzian, and Voigt profiles as models respectively, resulting in the corner plots (Foreman-Mackey, 2016) of Figures 6, and 7.

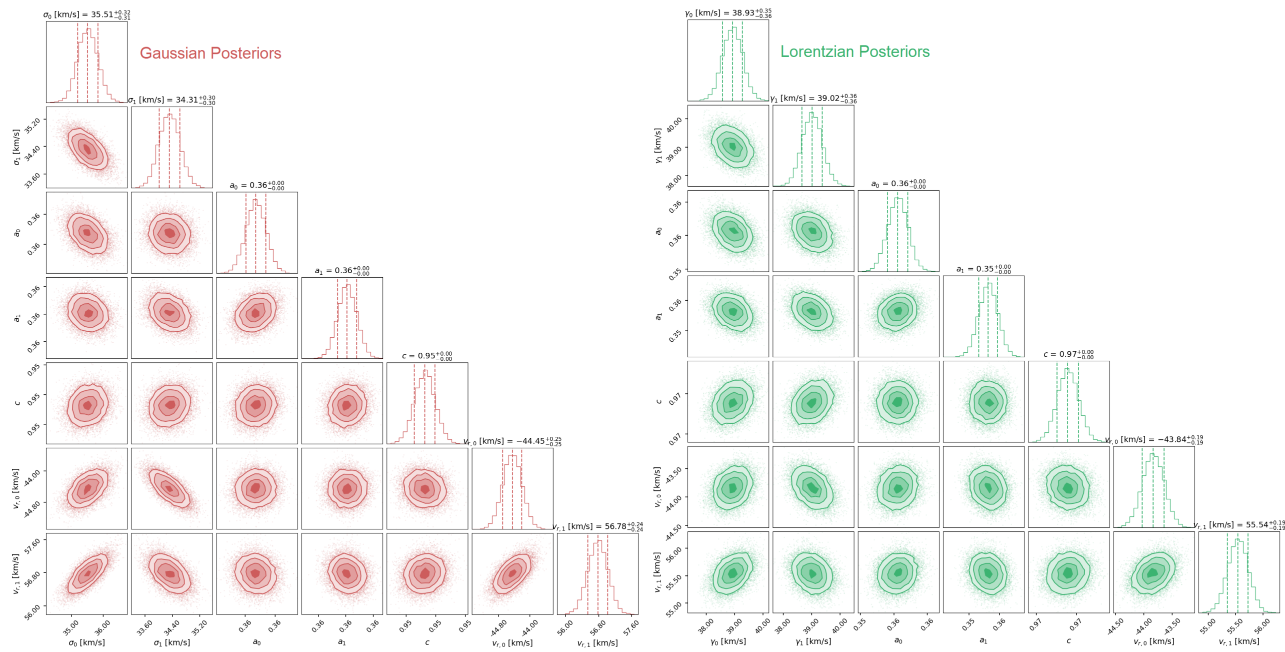

Figure 6: Left: posterior distribution for the parameters of the Gaussian profile, resulting from fitting a Gaussian profile for the Hα line at epoch 2019-05-12. Right: posterior distribution for the parameters of the Lorentzian profile, fit over the same feature at the same epoch. The parameters are as defined for Equations (5) and (6), with the exception of c, which is the continuum parameter. Indices of 0 refer to the parameters corresponding to the first spectral feature, i.e. the blueshifted feature, and indices 1 refer to the parameters corresponding to the second spectral feature, i.e. the redshifted feature.

Since the Gaussian and the Lorentzian functions utilize the same number of parameters, all of which have equivalent definitions, their posterior distributions look very similar. Nevertheless, based on the residuals visible in figure 7, it can be seen that the most accurate fitting profile is the Voigt line profile, and it is the Voigt peak positions which are thenceforth used to determine the radial velocities. Physically, the Voigt profile accounts for the line broadening mechanisms that the Gaussian profile and the Lorentzian profile individually describe, and thus such a profile can better describe the shape of stellar lines, in particular with regards to the wings of the lines.

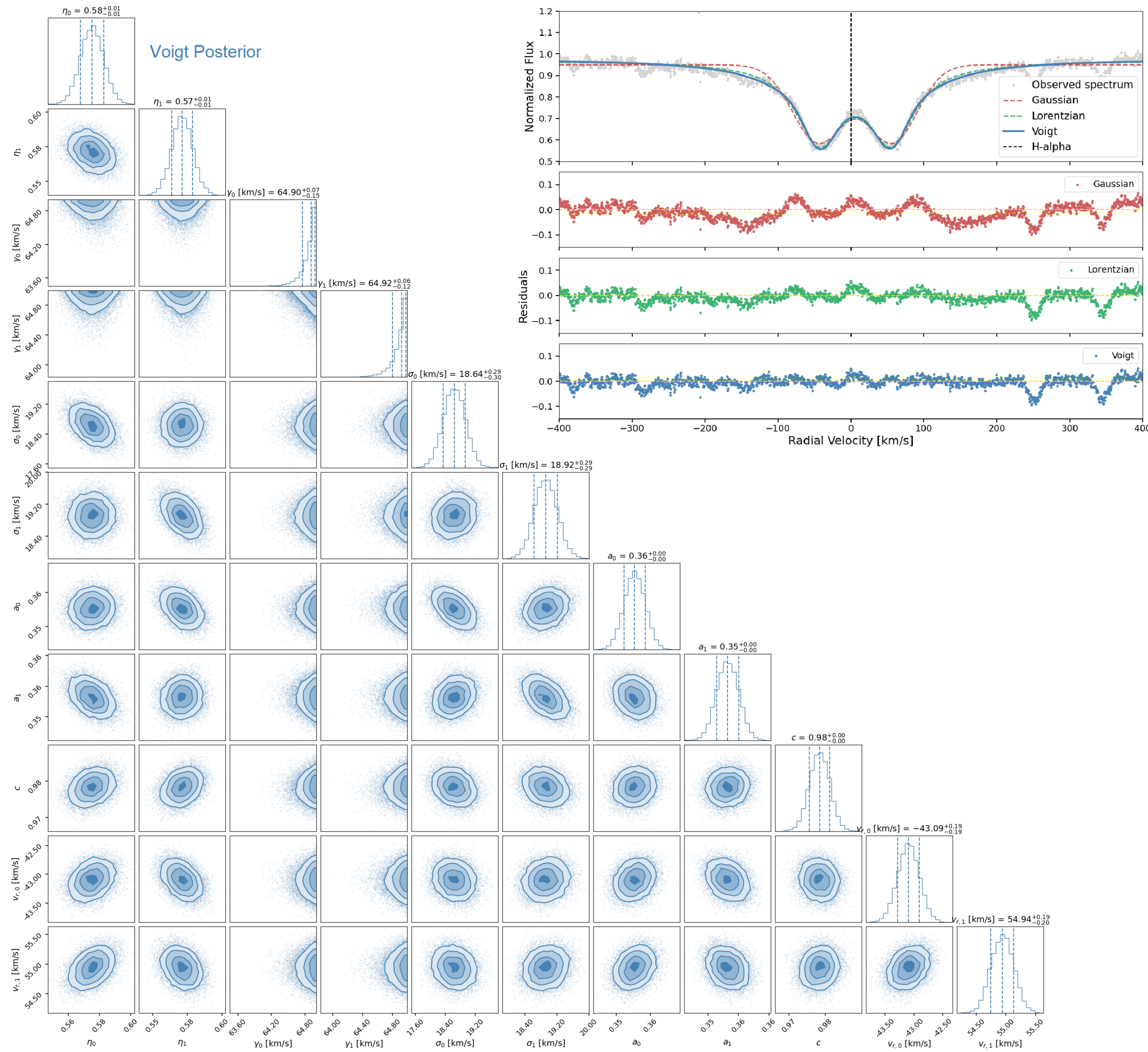

Figure 7: To the left is plotted the posterior distribution of the Voigt fit, for the same epoch as Figure 6. Top right is the subsequent plot for the epoch 2019-05-12, with corresponding Gaussian, Lorentzian, and Voigt best fits. The residuals are plotted underneath the fit results, which arise from subtracting each fit from the original spectrum. A horizontal line is plotted to denote the 0 value, and a vertical to signal $\lambda_{\mathrm{H}\alpha}$ in vacuum. Note that some features, such as those around $v_r = 250$ km/s, are other unfitted stellar lines, and therefore their presence in the residuals is not of concern. Indices of 0 denote the parameters for the first spectral feature, or the blueshifted feature, and indices of 1 denote the parameters for the second spectral feature, or the redshifted feature. The parameters are as defined for Equation (7), and c is the continuum parameter.

3.3 Keplerian Orbit Fitting

For producing the radial velocity over time curve of the two stellar components, every value of v_0 and v_1 for every stellar epoch originating from the fitting of the selected absorption features are saved, alongside their corresponding standard deviation. The weight of each radial velocity measurement is calculated as:

$$\text{weight} = \frac{1}{\text{error}^2}, \tag{16}$$

where the error is the standard deviation obtained from the posterior distributions. The average radial velocity of a stellar component for a given epoch then follows as an average of the values from the independent lines and their weights.

For fitting Equation (10) to the thus obtained radial velocity curve, another Markov chain Monte Carlo simulation is set up, where Equation (10) serves as the model, and the radial velocity data serve as the observation. What severely complicates the fitting, however, is the sparse dataset spread thinly over a very wide epoch range. This complicates the attribution of radial velocity values to one particular star. This would have been much easier to accomplish, provided there were radial velocity measurements over consecutive days, enabling one to track the change in measured values. In addition, the wide epoch range and sparse data can make the posterior distribution multimodal, due to how multiple parameter ranges being able to fit to some extent the radial velocity data.

To remedy these issue, a number of steps are taken. First, the MCMC fit is given some informative priors, based on what is deemed physical in terms of orbital dynamics. For instance, it was observed that at certain epochs there is a rapid change in measured radial velocity, where one star would go from a large positive RV to a negative RV within the span of a few days. This indicated that the orbit would be eccentric. At the same time, the systemic velocity γ was also restricted based on observations of a slight positive RV excess present in all measurements. The semi-amplitudes K_1 and K_2 are given very narrow ranges and non-uniform sampling additionally based on the observed maximal RV values measured throughout the dataset. Two additional error term are added, one for each star, σ_{jitter}, which expands the error range for the radial velocity measurements, and which accounts for uncertainties not captured by the model, as well as RV variability caused by stellar activity and noise.

Further, it is attempted to assign each radial velocity value to one respective star, thereby improving the observations for the model, as well as enabling better priors, based on line depths of unblended lines. It was observed visually that at some epochs when the features show the duplicated characteristic, that one line may be deeper than the other, which presumably is caused by slightly different properties of one star with regards to the other. Based on that, a preliminary classification is attempted. An illustration of this effort is made in Appendix 6.2.

3.4 Spectral Fitting with PySME

The software Spectroscopy Made Easy, specifically the python wrapper `pySME`[6] is used to fit a total of 32 selected segments over a wide spectral region going from $\lambda_{\text{min}} = 5860$ Å $\lambda_{\text{max}} = 6760$ Å (Wehrhahn et al., 2023). The fit is performed using the Gaia-ESO linelist (Heiter et al., 2021), where the elements outside the used segments have been cropped out for efficiency purposes. The primary complications that need to be handled are that the software cannot fit two stars at once from the same spectrum. Thus, the lines that are selected for the fit need to be so chosen that they clearly correspond to only one of the stars that is being fit. This is achieved by choosing lines at the same radial velocity shift. Still this is further complicated by the fact that some lines, even at large radial velocity separation, can be blended by other lines originating from the other star. Thus, at first only 32 segments were thought to be identified as not being contaminated with blends. Still, some might still be subject to blending.

In addition, there is a continuum problem that arises from the fact that both stars contribute to the continuum flux, while the separated doubled features remain individual contributions. This leads to absorption features that are half as intense relative to the continuum, which would skew the `pySME` fit towards unreasonably low values. In an attempt to remedy this, another continuum is fit over the selected wide region. This time, due to the spectrum having been flattened at normalization, as well as due to relatively fewer lines at the higher wavelength range, `np.polyfit` is used to generate the continuum in the form of a 3^{rd} degree polynomial, since it is comparatively easier to work with, and more complex functions are not needed. The higher degree is chosen so that the continuum curve retains some flexibility, and in order to compensate for a poorer continuum fit from the original normalization procedure, which resulted in a downwards tilt at the very end of the spectra. This continuum is then halved, and the result is subtracted from the spectrum. This, it is hoped, restores the ratio of the absorption features relative to the continuum.

The chosen region is presented in Figure 8, and the list of segments used into the `pySME` solver are presented in Table 3. In total, once the segments are used to mask the outside regions out of the fit, 7104 pixels within the `sme` structure are used. The aim is to use as many lines as is computationally effective, to maximise the probability that the solver will have enough data to arrive at reliable results, keeping in mind the computational costs of fitting many lines at once.

The segments in Table 3 were initially selected by comparing the spectrum for an epoch where the lines were far apart with one where the lines were blended. In particular, for Table 3 they correspond with segments chosen for the epoch 2019-07-14, for which Doppler shifted lines could be identified with their rest RV at an epoch where they were blended. In order to perform the fit for multiple epochs, knowing the radial velocity shifts corresponding to 2019-07-14 (for example from the tabulated values in Appendix 6.1), one can shift those segments into the rest wavelength, and then into the observed wavelength corresponding to any of the available epochs. One such particular epoch that is subsequently presented in Results is 2019-07-13. It is for this epoch that the spectral window with the chosen segments used in the `pySME` fit are illustrated in Figure 8.

[6] https://pysme-astro.readthedocs.io/en/stable/

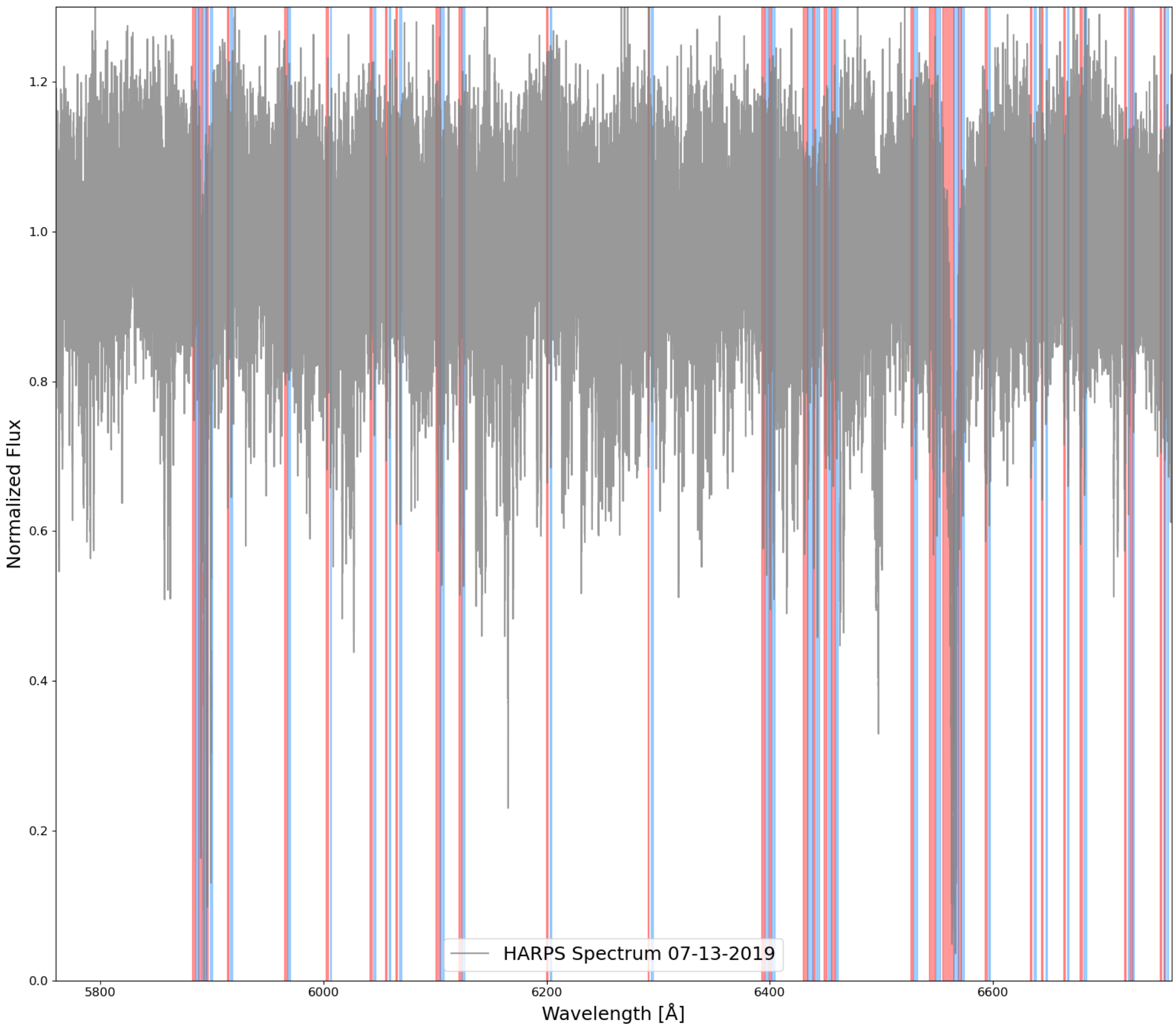

Figure 8: Plot of the spectral range used for the internal parameter fitting. The segments capturing the absorption features used in the solver are highlighted in blue for star 1, and in red for star 2 respectively.

With this dataset, the `pySME` solver is initialized to fit for effective temperature $T_{\rm eff}$, surface gravity $\log g$, metallicity monh, stellar rotational broadening $v \sin i$, and radial velocity $v_{\rm rad}$. The last term is primarily to check that the solver does not fit the undesired spectral features. A good $v_{\rm rad}$ for a given spectrum would be one approximately equal to the radial velocity fitted through the Voigt profile fitting previously for that same spectrum and epoch.

λ_{start}, Star 1 [Å]	λ_{end}, Star 1 [Å]	λ_{start}, Star 2 [Å]	λ_{end}, Star 2 [Å]
5882.30	5885.40	5886.00	5887.90
5887.90	5890.80	5891.90	5894.80
5894.70	5896.70	5898.20	5900.40
5913.50	5915.00	5916.70	5918.30
5965.11	5967.28	5968.31	5970.24
6001.81	6003.88	6005.86	6006.94
6041.58	6043.47	6045.00	6046.94
6055.28	6056.74	6058.61	6060.30
6064.63	6066.01	6067.90	6069.77
6100.80	6104.30	6104.40	6107.60
6121.10	6124.00	6124.40	6126.40
6199.60	6201.00	6203.00	6204.30
6290.38	6291.43	6293.58	6295.33
6392.30	6395.30	6395.90	6398.50
6399.00	6401.10	6401.90	6404.20
6429.82	6433.30	6433.53	6438.00
6437.96	6440.00	6441.29	6444.28
6448.38	6451.14	6452.03	6454.76
6454.64	6458.17	6458.56	6460.65
6525.68	6528.28	6528.92	6532.11
6542.72	6548.20	6548.61	6552.91
6560.87	6564.79	6564.77	6568.47
6592.16	6594.62	6595.69	6597.23
6632.88	6634.64	6636.51	6638.47
6643.25	6644.40	6646.94	6648.05
6662.79	6664.21	6666.25	6667.86
6677.43	6679.26	6680.79	6683.28
6707.71	6708.38	6711.15	6712.35
6717.17	6718.58	6721.06	6722.31
6722.91	6724.67	6725.04	6726.31
6749.65	6751.02	6753.43	6754.43
6752.42	6753.40	6755.82	6756.91

Table 3: The spectral segments used in Figure 8, with their corresponding start and end wavelengths.

4 Results

4.1 Radial Velocity Measurements

The extracted radial velocity measurements for the selected lines are presented in Tables 6, 7, and 8 in Appendix 6.1. In addition, the averaged radial velocity measurements are plotted in Figure 9. The variability in radial velocities over time within the chosen features is can be seen, further suggesting the idea that the stellar system is a dynamic binary system of stars in orbit around each other. These measurements also anticipate one difficulty in fitting the Keplerian orbits, namely that many measurements are clustered around short time intervals, with long breaks in between time clusters. This discontinuity makes it more difficult to accurately determine the period P and eccentricity e of the system.

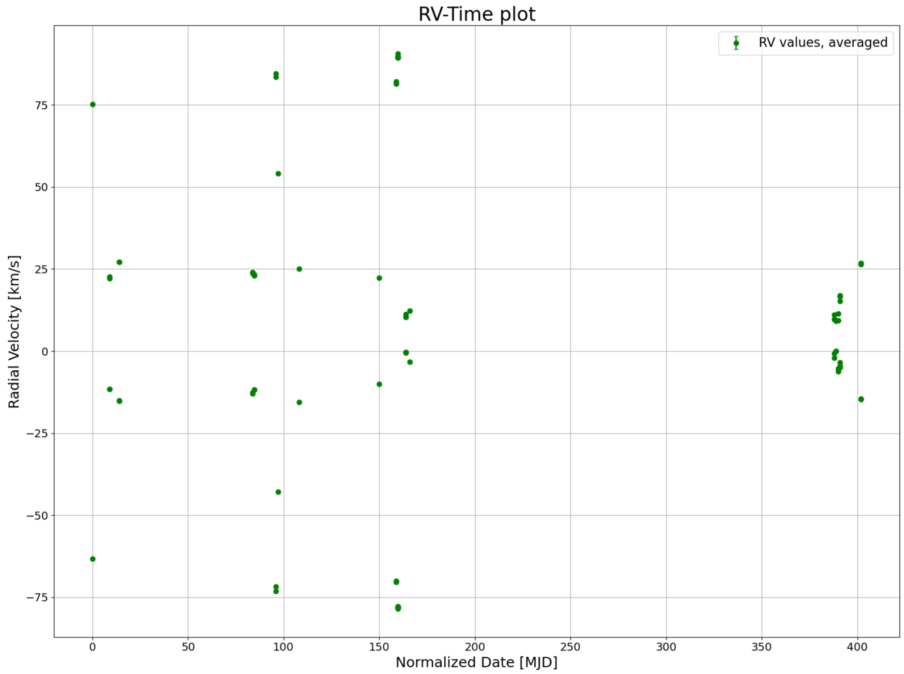

Figure 9: RV-time plot obtained from the measured radial velocity values. The measurements are a result of a weighted average between the values obtained from the selected lines discussed previously. The time has been converted to Modified Julian Dates, and then zero'd at the first epoch. Note that the values have associated uncertainties, however due to the scale of the plot, they are not visible.

4.2 Keplerian Orbit Fitting

From the averaged values of Tables 6, 7, and 8, the radial velocities of the two stars at different epochs are determined. A classification is attempted as illustrated in Appendix 6.2. The posterior distribution of the orbital parameters used in the determination of the orbits, alongside the model radial velocity curves drawn from those posteriors, can be seen in Figure 10. To note that not all the points plotted in Figure 9 ended up being used in the fit of Figure 10. The principal reason for the exclusion of some points was the inability to classify them as belonging to either star 1 or star 2 based on different line depths. Additionally, data points with radial velocities close to zero were also omitted, since they featured blended lines where classification could also not be performed. As such, some points were omitted from the final radial velocity set used for the fit. This exclusion concerns, in particular, also the datapoints at the last epochs around 400 MJD. Fortunately this avoids having to attempt the fit with a large gap of about 200 days in the dataset. Normally, this should not lead to significant problems, as the final fit contains a similarly large gap of roughly 80 days anyway. It could, however, make the fitting algorithm slower, and if the datapoints were more sparse, could lead to difficulties in converging to solutions for the period and eccentricity.

Figure 10 suggests a highly eccentric binary orbit, with period of roughly $P = 23 \pm 2\%$ days, between stars of similar mass with mass ratio q close to unity $\pm 7\%$. Due to a lack of known value for the inclination of the orbit, the individual masses of the stars cannot readily be determined. In addition, for the precise calculation of the individual masses, it is necessary to constrain the semi-amplitudes K_1 and K_2. It becomes apparent that better-timed measurements are needed in order more accurately characterise the binary system. Improvements will be discussed in Outlook and Future Work.

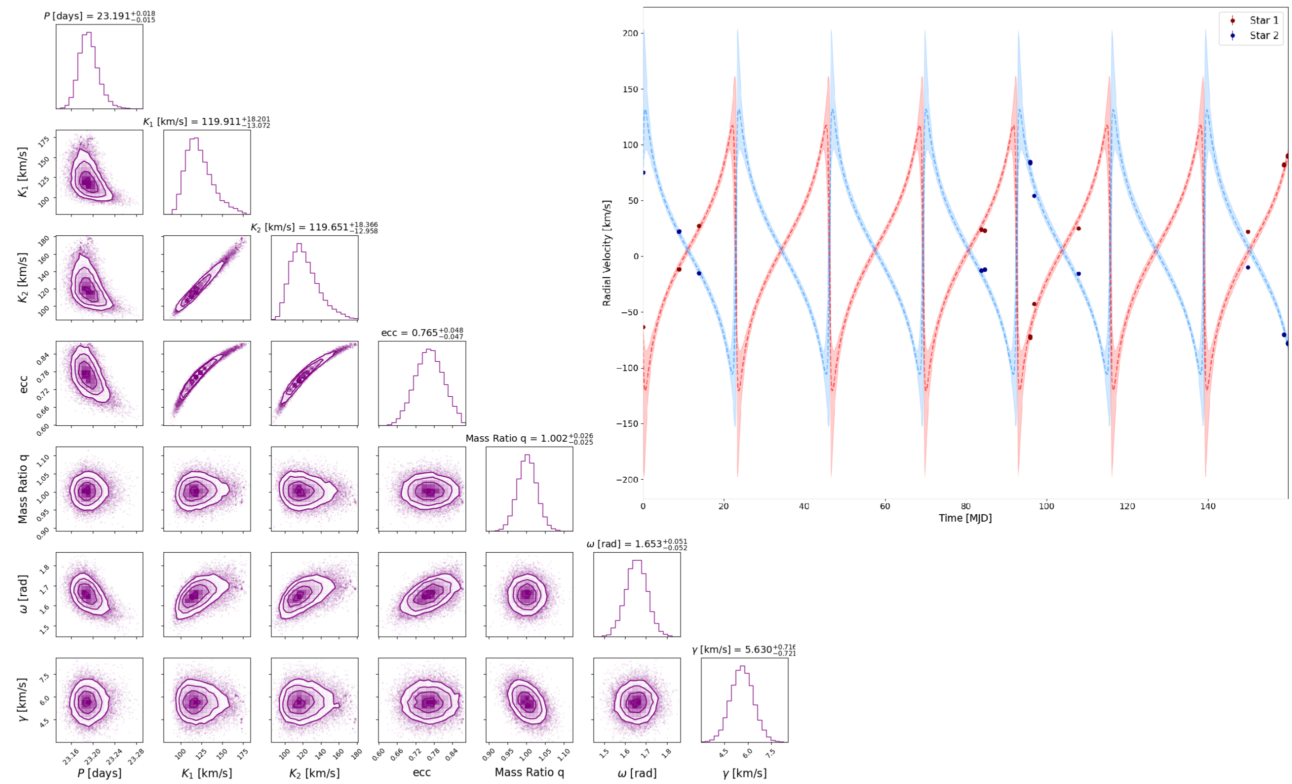

Figure 10: Posterior distribution following the fit of the radial velocity equation (10) with the collected radial velocity data. From this posterior distribution, the mean is used to overplot the model RV curve over the data points. The shaded regions represent the 3σ spread drawn from the distribution, while the dashed lines represent the mean fit solution. Note that the posterior mass ratio q is drawn from the mean. The median is calculated as $q = 1.001 \pm 7\%$. Also note that the error bars of the radial velocity measurements are too small relative to the scale of the plot.

For stars of roughly equal masses, such an eccentric system is perhaps expected given that the gravitational contribution of the stars will be about the same, each affecting the other more or less equally. In that regard it is perhaps similar to how more massive, close-in exoplanets will displace their host star from the true center of mass of the system by a greater amount. A comparison can further be drawn with the αCen AB system, where 2 stars of roughly the same mass are drawn into an eccentric orbit of about $e = 0.51947 \pm 0.00015$ (Akeson et al., 2021).

4.3 Internal Stellar Parameters

Via the `pySME` solver, synthetic spectra could be generated and fit over the data described in Figure 8 and Table 3. The resulting spectra are presented in Figures 11 and 12.

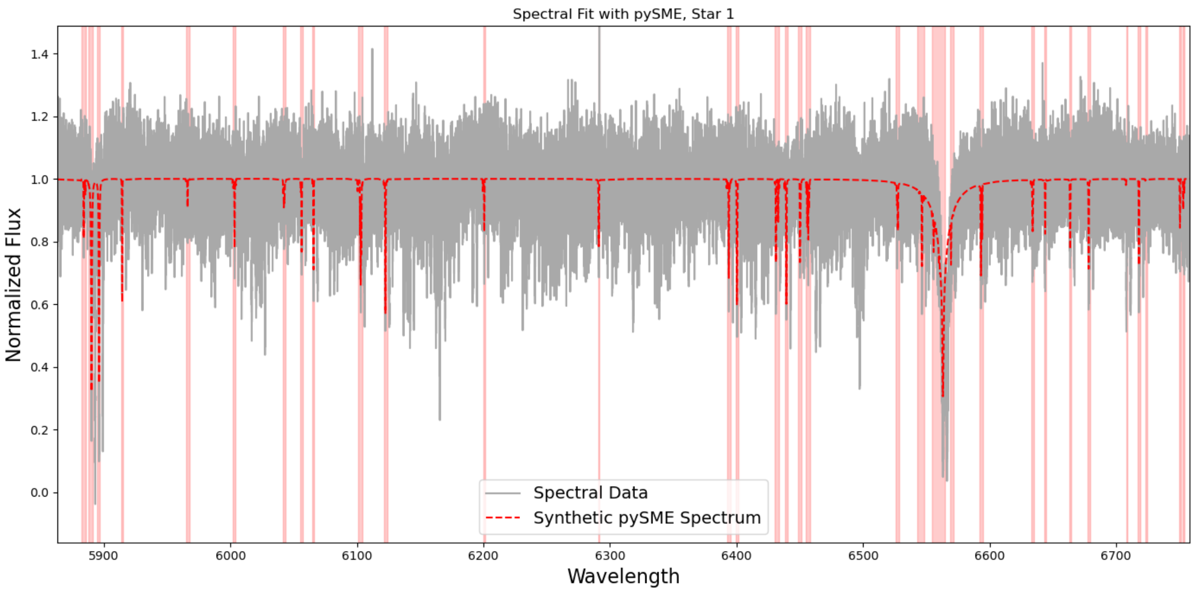

Figure 11: Synthetic spectrum resulting from the SME solver for the dataset corresponding to star 1 for epoch 2019-07-13. In gray dots is represented the observed flux used as the data. In shaded regions are the segments included in the fit. The wavelength is given in [Å].

The synthetic spectrum in Figure 11 was generated based on the resolved the parameters in Table 4, given by the solver. It should be noted that based on those values, star 1 appears to be more of an F-type star rather than the literature G-type commonly attributed to the system. At the same time, however, the $\log g$ value appears unusually high for an F-type star. An F-type star would indicate a more massive star, but at the same time also a star of larger radius.

Parameter	Value
T_{eff} [K]	6390.3198 ± 16.3613
$\log g$ [cms^{-2}]	4.8177 ± 0.0410
Metallicity [Relative to Sun]	0.2814 ± 0.0174
$v \sin i$ [km/s]	9.7144 ± 0.2088

Table 4: Table of final fit parameters used to generate the synthetic spectrum overplotted in Figure 11.

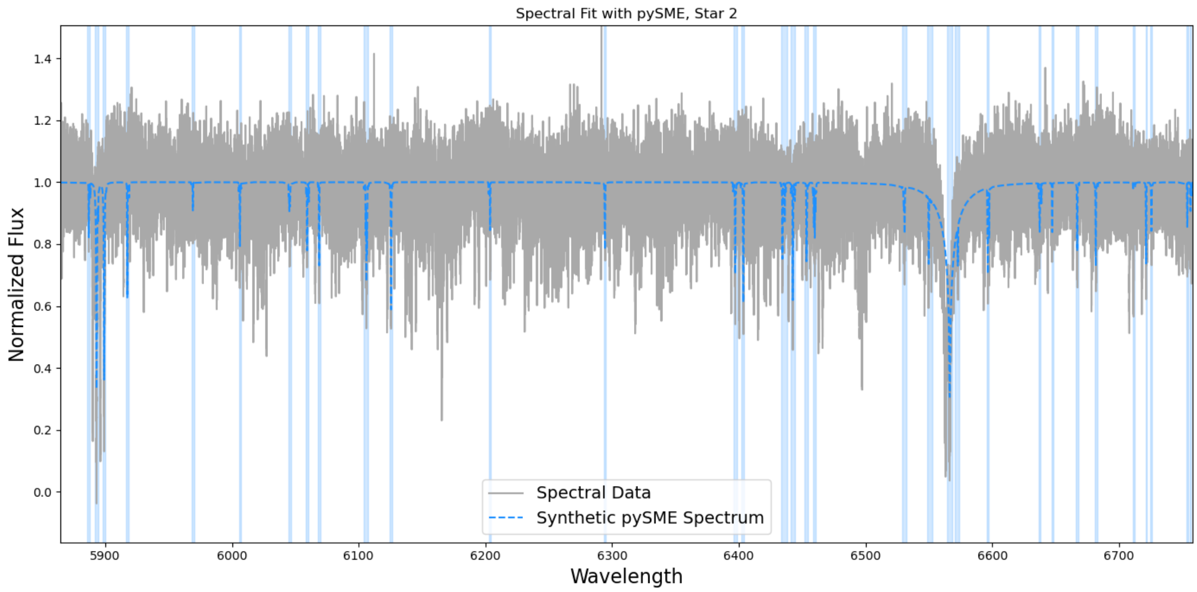

Figure 12: Synthetic spectrum resulting from the SME solver for the dataset corresponding to star 2 for the epoch 2019-07-13. In gray dots is represented the observed flux used as the data. In shaded regions are the segments included in the fit. The wavelength is given in [Å].

Similar to the first synthetic spectrum, the synthetic spectrum for star 2 was generated from the `SME` solver following the fitting of stellar parameters to the selected spectral regions. The results are highlighted in Table 5. It can be noted that the obtained values are similar to star 1, which is consistent with the initial observation obtained from the Keplerian orbit, namely that the stars are of similar mass, and consequently should be of a similar type given that they are expected to have been born at around the same time. Again we observe the unusually high $\log g$ value, and again it is indicated by the fitted effective temperature that this star too would correspond to an F-type star, rather than a G-type.

Parameter	Value
T_{eff} [K]	6424.3609 ± 20.3072
$\log g$ [cms^{-2}]	4.8742 ± 0.040
Metallicity [Relative to Sun]	0.3493 ± 0.0181
$v \sin i$ [km/s]	11.1686 ± 0.2263

Table 5: Table of final fit parameters used to generate the synthetic spectrum overplotted in Figure 12.

For both Figures 11 and 5, zoomed in plots are presented in Appendix 6.3. Additionally it was observed that performing the fitting procedure while excluding the Hα and NaI D lines, the measured values would be considerably lower, where the resulting fits are presented in Figures 13 and 14.

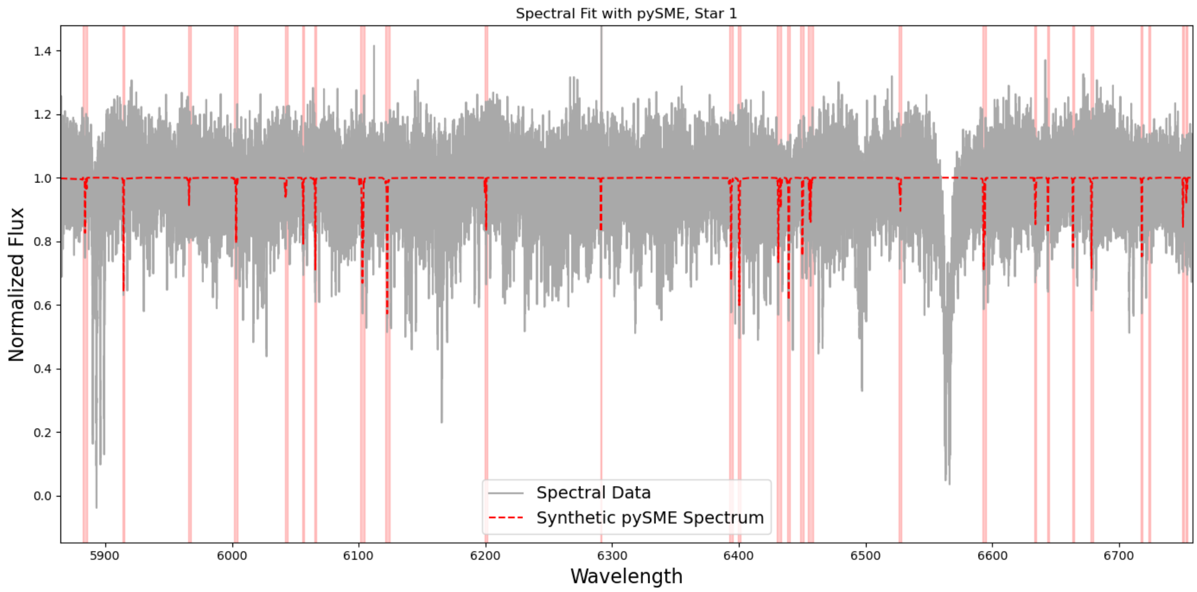

Figure 13: Synthetic spectrum resulting from the SME solver for the dataset corresponding to star 1 for the epoch 2019-07-13, excluding the Hα and NaI D lines. In gray dots is represented the observed flux used as the data. In shaded regions are the segments included in the fit. The wavelength is given in [Å].

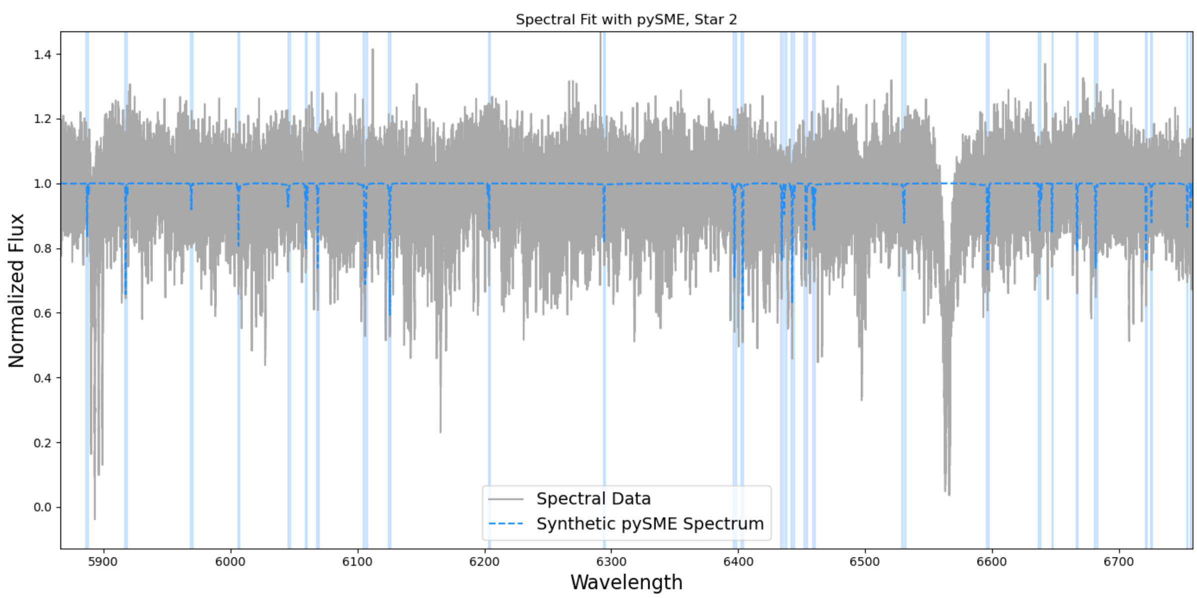

Figure 14: Synthetic spectrum resulting from the SME solver for the dataset corresponding to star 2 for the epoch 2019-07-13, excluding the Hα and NaI D lines. In gray dots is represented the observed flux used as the data. In shaded regions are the segments included in the fit. The wavelength is given in [Å].

For instance, it is observed that the effective temperatures drop to $T_{\text{eff},1} = 5856.9168 \pm 37.6081$ K, and $T_{\text{eff},2} = 6211.8745 \pm 40.6190$ K. This is probably due to the excluded lines being good indicators of temperature, particularly the wings of the Hα line. This also reduces the $\log g$ values, although not significantly. The measured metallicities are another curious parameter. It is expected that the metallicities of the two stars should be the same, given that they are born out of the same dust at around the same time, yet one star presents a higher metallicity. It is unclear whether this is accurate, or simply an artefact of the fit. Such difficulties from the fit could arise from the selection of bad pixels, i.e. segments that are not useful for the solver to determine these parameters.

5 Outlook and Future Work

Overall the results confirm the suspicion first enunciated in Grandjean et al., 2023, namely that HD 129590 is indeed a binary system. Moreover, it appears to be a highly eccentric system, with almost equally massive planets orbiting in a close orbit around their center of mass. This perhaps unusual configuration could have interesting implications for the observed debris disk. In particular, it would be interesting to investigate the long-term stability of such a system, or if planetary systems could develop in such situations. One can imagine that stellar objects on highly eccentric objects could pull inwards material that is on the outer edges of the system, and in so doing bring exocometary material from the outskirts of the system down into an inner orbit. To that end, N-body simulations of this system could be particularly well-suited to investigate these dynamics.

As can be observed in Figure 10, in particular the semi-amplitudes K_1 and K_2 are not very well constrained. That is because the archival data used in this project did not have consecutive datapoints at and around the maxima and minima of the amplitudes, and thus the exact K values could not be very well determined. This is especially difficult since the system appears to be quite eccentric, meaning that there is only a very brief interval at which the stars sit at these maxima and minima K values. More measurements, and in particular consecutively timed, could improve the orbital fit significantly. It could be worth investigating the light curves of this system with the Transiting Exoplanet Survey Satellite (TESS), although this depends on the system being an eclipsing binary, which is uncertain. Should it be one, however, such light curves could help determine the exact period of this system.

5.1 Conclusion

Contrary to established literature (e.g. Chen et al., 2011), results indicate that the HD 129590 system is in actuality a binary system comprised of essentially equally massive stars on highly eccentric orbits and short periods around the system's center of mass. The fitting of internal parameters of the stars reveal stars of similar parameters with the indication that they are F-type stars. These findings reveal a highly dynamic and complex system, with potential implications to the debris disk it possesses. A deeper understanding of the overall dynamics and stability of the system would welcome the dynamical simulation of the debris disk, with its components, around the stellar system thus described. Perhaps most excitingly, it would be interesting to see if zones of stability around this eccentric binary system could exist for planets to develop, which in turn could serve as first clues in future searches for exoplanets in similar systems.

References

Akeson, R., Beichman, C., Kervella, P., Fomalont, E., & Benedict, G. F. (2021). Precision Millimeter Astrometry of the α Centauri AB System. *The Astronomical Journal*, *162*(1), Article 14, 14. https://doi.org/10.3847/1538-3881/abfaff

Apellániz, J. M., Negueruela, I., & Caballero, J. A. (2024). Spectral classification. https://arxiv.org/abs/2410.07301

Barragán, O., Gandolfi, D., & Antoniciello, G. (2019). PYANETI: a fast and powerful software suite for multiplanet radial velocity and transit fitting. *Monthly Notices of the Royal Astronomical Society*, *482*(1), 1017–1030. https://doi.org/10.1093/mnras/sty2472

Bayes, T. (1763). Lii. an essay towards solving a problem in the doctrine of chances. by the late rev. mr. bayes, f. r. s. communicated by mr. price, in a letter to john canton, a. m. f. r. s. *Philosophical Transactions*, (53), 370–418. https://doi.org/10.1098/rstl.1763.0053

Bingham, E., Chen, J. P., Jankowiak, M., Obermeyer, F., Pradhan, N., Karaletsos, T., Singh, R., Szerlip, P. A., Horsfall, P., & Goodman, N. D. (2019). Pyro: Deep universal probabilistic programming. *J. Mach. Learn. Res.*, *20*, 28:1–28:6. http://jmlr.org/papers/v20/18-403.html

Blaauw, A. (1946). A Study of the Scorpio-Centaurus Cluster. *Publications of the Kapteyn Astronomical Laboratory Groningen*, *52*, 1–132.

Bradbury, J., Frostig, R., Hawkins, P., Johnson, M. J., Leary, C., Maclaurin, D., Necula, G., Paszke, A., VanderPlas, J., Wanderman-Milne, S., & Zhang, Q. (2018). JAX: Composable transformations of Python+NumPy programs. http://github.com/jax-ml/jax

Burt, J. A., Dumusque, X., & Halverson, S. (2025). Precise radial velocities. https://arxiv.org/abs/2511.01954

Cannon, A. J., & Pickering, E. C. (1918). The Henry Draper catalogue 0h, 1h, 2h, and 3h. *Annals of Harvard College Observatory*, *91*, 1–290.

Chen, C. H., Mamajek, E. E., Bitner, M. A., Pecaut, M., Su, K. Y., & Weinberger, A. J. (2011). A magellan mike and spitzer mips study of 1.5-1.0 m_{sun} stars in scorpius-centaurus. *The Astrophysical Journal*, *738*(2), Article 122, 122. https://doi.org/10.1088/0004-637X/738/2/122

Earl, N., O'Steen, R., Tollerud, E., brechmos, Kerzendorf, W., Busko, I., Lim, P. L., shaileshahuja, D'Avella, D., Robitaille, T., Ginsburg, A., Homeier, D., Sipőcz, B., Averbukh, J., Cherinka, B., Tocknell, J., Ogaz, S., Geda, R., Davies, J., … Ferguson, H. (2026, February). *Astropy/specutils: V2.3.0* (Version v2.3.0). Zenodo. https://doi.org/10.5281/zenodo.18473282

Fang, M., & Herczeg, G. J. (2025). A Comprehensive Gaia Spectroscopic Study of Stars in the Scorpius-Centaurus Complex: Star Formation History and Disk Lifetime. *The Astrophysical Journal*, *994*(2), Article 248, 248. https://doi.org/10.3847/1538-4357/ae0f9a

Foreman-Mackey, D. (2016). Corner.py: Scatterplot matrices in python. *The Journal of Open Source Software*, *1*(2), 24. https://doi.org/10.21105/joss.00024

Grandjean, A., Lagrange, A.-M., Meunier, N., Chauvin, G., Borgniet, S., Desidera, S., Galland, F., Kiefer, F., Messina, S., Iglesias, D., Nicholson, B., Pantoja, B., Rubini, P., Sedaghati, E., Sterzik, M., & Zicher, N. (2023). HARPS radial velocity search for planets in the Scorpius-Centaurus association. A combination with the HARPS and SOPHIE young nearby stars (YNS) surveys. *Astronomy & Astrophysics*, *669*, Article A12, A12. https://doi.org/10.1051/0004-6361/202141235

Heiter, U., Lind, K., Bergemann, M., Asplund, M., Mikolaitis, Š., Barklem, P. S., Masseron, T., de Laverny, P., Magrini, L., Edvardsson, B., Jönsson, H., Pickering, J. C., Ryde, N., Bayo Arán, A., Bensby, T., Casey, A. R., Feltzing, S., Jofré, P., Korn, A. J., . . . Gilmore, G. F. (2021). Atomic data for the Gaia-ESO Survey. *Astronomy & Astrophysics*, *645*, Article A106, A106. https://doi.org/10.1051/0004-6361/201936291

Ida, T., Ando, M., & Toraya, H. (2000). Extended pseudo-voigt function for approximating the voigt profile. *Journal of Applied Crystallography*, *33*(6), 1311–1316. https://doi.org/https://doi.org/10.1107/S0021889800010219

Ivezić, Ž., Connolly, A. J., VanderPlas, J. T., & Gray, A. (2014). Bayesian statistical inference. In *Statistics, data mining, and machine learning in astronomy: A practical python guide for the analysis of survey data* (STU - Student edition, pp. 175–246). Princeton University Press. Retrieved May 3, 2026, from http://www.jstor.org/stable/j.ctt4cgbdj.8

Karttunen, H., Kröger, P., Oja, H., Poutanen, M., & Donner, K. J. (2017). *Fundamental Astronomy*. https://doi.org/10.1007/978-3-662-53045-0

Kral, Q., Matrà, L., Kennedy, G. M., Marino, S., & Wyatt, M. C. (2020). Survey of planetesimal belts with ALMA: gas detected around the Sun-like star HD 129590. *Monthly Notices of the Royal Astronomical Society*, *497*(3), 2811–2830. https://doi.org/10.1093/mnras/staa2038

Kramida, A., Ralchenko, Y., Reader, J., & Team, N. A. (2023). Nist atomic spectra database (ver. 5.12) [National Institute of Standards and Technology, Gaithersburg, MD].

Mamajek, E. E., Meyer, M. R., & Liebert, J. (2002). Post-t tauri stars in the nearest ob association. *The Astronomical Journal*, *124*(3), 1670. https://doi.org/10.1086/341952

Matthews, E., Hinkley, S., Vigan, A., Kennedy, G., Rizzuto, A., Stapelfeldt, K., Mawet, D., Booth, M., Chen, C., & Jang-Condell, H. (2017). The First Scattered-light Image of the Debris Disk around the Sco-Cen Target HD 129590. *The Astrophysical Journal Letters*, *843*(1), Article L12, L12. https://doi.org/10.3847/2041-8213/aa7943

Olofsson, J., Thébault, P., Bayo, A., Henning, T., & Milli, J. (2024). The near-infrared degree of polarization in debris disks. Toward a self-consistent approach to model scattered light observations. *Astronomy & Astrophysics*, *688*, Article A42, A42. https://doi.org/10.1051/0004-6361/202450100

Olofsson, J., Thébault, P., Bayo, A., Milli, J., van Holstein, R. G., Henning, T., Medina-Olea, B., Godoy, N., & Maucó, K. (2023). Apocenter pileup and arcs: A narrow dust ring around HD 129590. *Astronomy & Astrophysics*, *674*, Article A84, A84. https://doi.org/10.1051/0004-6361/202346097

Pearce, T. D. (2026). Debris disks around main-sequence stars. *Encyclopedia of Astrophysics, Volume 1*, *1*, 270–287. https://doi.org/10.1016/B978-0-443-21439-4.00014-6

Pepe, F., Mayor, M., Delabre, B., Kohler, D., Lacroix, D., Queloz, D., Udry, S., Benz, W., Bertaux, J.-L., & Sivan, J.-P. (2000, August). HARPS: a new high-resolution spectrograph for the search of extrasolar planets. In M. Iye & A. F. Moorwood (Eds.), *Optical and ir telescope instrumentation and detectors* (pp. 582–592, Vol. 4008). https://doi.org/10.1117/12.395516

Phan, D., Pradhan, N., & Jankowiak, M. (2019). Composable effects for flexible and accelerated probabilistic programming in numpyro. *arXiv preprint arXiv:1912.11554*.

Rybicki, G. B., & Lightman, A. P. (1979). *Radiative processes in astrophysics*.

Smette, A., Sana, H., Noll, S., Horst, H., Kausch, W., Kimeswenger, S., Barden, M., Szyszka, C., Jones, A. M., Gallenne, A., Vinther, J., Ballester, P., & Taylor, J. (2015). Molecfit: A general tool for telluric absorption correction. I. Method and application to ESO instruments. *Astronomy & Astrophysics*, *576*, Article A77, A77. https://doi.org/10.1051/0004-6361/201423932

Stein, T., Krivov, A. V., & Löhne, T. (2026). How hard is dust in debris disks? *Astronomy & Astrophysics*, *707*, Article A351, A351. https://doi.org/10.1051/0004-6361/202558500

Wehrhahn, A., Piskunov, N., & Ryabchikova, T. (2023). PySME. Spectroscopy Made Easier. *Astronomy & Astrophysics*, *671*, Article A171, A171. https://doi.org/10.1051/0004-6361/202244482

Wright, N. J. (2020). OB Associations and their origins. *New Astronomy Reviews*, *90*, Article 101549, 101549. https://doi.org/10.1016/j.newar.2020.101549

6 Appendix

6.1 Tabulated Radial Velocity Measurements

Date	Fe I Line at 5885.447 Å				Fe I Line at 6057.681 Å			
	v_0 [km/s]		v_1 [km/s]		v_0 [km/s]		v_1 [km/s]	
	Mean	Std	Mean	Std	Mean	Std	Mean	Std
2019-02-04	−62.63	0.27	74.23	0.29	−62.21	0.36	75.21	0.29
2019-02-13	−12.47	0.50	23.35	0.49	−11.56	0.42	24.06	0.53
2019-02-13	−11.17	0.44	23.25	0.45	−11.25	0.43	23.26	0.35
2019-02-18	−15.48	0.21	26.77	0.20	−14.93	0.18	27.20	0.20
2019-02-18	−15.68	0.23	26.96	0.19	−15.20	0.18	27.85	0.20
2019-04-29	−13.02	0.23	24.41	0.19	−12.42	0.21	24.44	0.21
2019-04-29	−12.58	0.20	24.42	0.20	−12.50	0.22	24.82	0.19
2019-04-30	−11.61	0.23	23.25	0.19	−11.47	0.20	23.28	0.18
2019-04-30	−11.42	0.20	23.28	0.18	−11.57	0.18	23.48	0.18
2019-05-11	−73.02	0.37	83.56	0.37	−73.70	0.34	84.02	0.38
2019-05-11	−70.91	0.28	82.66	0.35	−72.57	0.28	82.71	0.30
2019-05-12	−42.08	0.32	52.28	0.34	−42.76	0.28	53.16	0.32
2019-05-23	−14.14	0.29	26.62	0.28	−14.65	0.29	27.02	0.33
2019-07-04	−10.49	0.52	22.26	0.42	−10.32	0.53	22.19	0.37
2019-07-13	−69.84	0.67	78.34	0.89	−70.33	0.57	83.19	0.66
2019-07-13	−70.77	1.09	79.55	0.85	−69.99	1.38	81.53	0.85
2019-07-13	−70.02	0.82	80.44	0.95	−70.90	0.57	81.43	0.62
2019-07-14	−78.58	0.59	90.68	0.76	−77.80	0.54	90.55	0.53
2019-07-14	−79.11	0.74	87.96	0.81	−78.11	0.58	87.91	0.86
2019-07-14	−80.17	0.53	89.98	0.65	−77.45	0.52	87.45	0.64
2019-07-14	−78.07	0.55	89.39	0.81	−77.81	0.42	87.74	0.48
2019-07-14	−78.82	0.60	89.56	0.73	−77.78	0.39	88.86	0.52
2019-07-14	−79.25	0.64	88.52	0.74	−77.71	0.41	87.66	0.65
2019-07-18	−0.61	0.52	8.32	0.86	−2.41	1.56	7.98	0.93
2019-07-18	−0.89	0.38	7.07	0.88	−1.06	0.85	8.06	0.72
2019-07-18	−0.36	0.42	7.97	0.92	−0.39	0.40	8.33	0.57
2019-07-20	−3.42	1.36	12.42	1.50	−5.65	2.05	11.51	1.74
2020-02-27	−0.31	0.30	9.66	0.91	−1.28	0.78	9.29	0.81
2020-02-27	−0.59	0.64	8.78	0.42	−1.24	1.10	8.84	1.10
2020-02-28	−0.77	0.44	8.39	0.38	−1.90	0.54	7.53	0.35
2020-02-28	−0.42	0.29	8.32	0.30	−0.60	0.45	8.32	0.43
2020-02-29	−4.16	0.59	9.00	0.50	−7.19	0.26	7.66	0.34
2020-02-29	−5.10	0.85	7.99	0.56	−3.39	1.26	10.54	1.02
2020-03-01	−3.69	0.52	16.71	0.40	−4.95	0.37	16.23	0.35
2020-03-01	−4.18	0.49	16.73	0.49	−4.81	0.61	16.18	0.57
2020-03-01	−5.67	0.41	16.64	0.32	−5.77	0.43	16.62	0.36
2020-03-01	−5.12	0.36	16.90	0.30	−5.80	0.45	16.79	0.37
2020-03-12	−14.77	0.29	27.09	0.23	−14.60	0.25	26.89	0.25
2020-03-12	−14.74	0.33	26.34	0.21	−14.54	0.24	26.88	0.23

Table 6: Extracted mean radial velocity measurements and their standard deviations, obtained from posterior distributions of fit Voigt profiles for the absorption features at 5885.447 Å and 6057.681 Å.

Date	Fe I Line at 6067.161 Å				Fe I Line at 6548.047 Å			
	v_0 [km/s]		v_1 [km/s]		v_0 [km/s]		v_1 [km/s]	
	Mean	Std	Mean	Std	Mean	Std	Mean	Std
2019-02-04	−62.70	0.16	74.76	0.18	−63.31	0.22	74.47	0.22
2019-02-13	−11.80	0.31	23.86	0.28	−10.52	0.35	23.80	0.33
2019-02-13	−12.07	0.27	23.54	0.25	−11.26	0.33	23.36	0.29
2019-02-18	−15.10	0.12	27.31	0.12	−14.92	0.17	27.28	0.15
2019-02-18	−15.26	0.11	27.45	0.12	−15.08	0.17	27.48	0.14
2019-04-29	−12.61	0.13	25.09	0.12	−12.65	0.18	25.13	0.17
2019-04-29	−12.88	0.13	25.00	0.11	−13.15	0.17	24.72	0.16
2019-04-30	−11.86	0.11	23.79	0.11	−12.07	0.16	24.29	0.15
2019-04-30	−11.90	0.11	23.91	0.11	−11.93	0.15	24.14	0.15
2019-05-11	−72.78	0.23	84.30	0.24	−73.29	0.27	84.49	0.33
2019-05-11	−70.90	0.20	82.61	0.19	−71.83	0.24	82.80	0.24
2019-05-12	−41.73	0.17	52.94	0.18	−41.56	0.21	52.58	0.23
2019-05-23	−13.98	0.18	24.98	0.02	−13.84	0.28	26.76	0.23
2019-07-04	−9.73	0.26	21.79	0.25	−10.47	0.38	22.38	0.27
2019-07-13	−70.28	0.43	80.27	0.37	−71.36	0.47	80.97	0.59
2019-07-13	−69.34	0.43	81.20	0.45	−69.89	0.51	78.59	0.58
2019-07-13	−68.13	0.36	81.42	0.40	−70.36	0.50	80.97	0.73
2019-07-14	−78.09	0.39	89.34	0.39	−78.08	0.48	88.38	0.71
2019-07-14	−78.73	0.48	89.38	0.49	−79.34	0.43	88.77	0.80
2019-07-14	−78.30	0.33	88.54	0.37	−78.62	0.45	91.33	0.48
2019-07-14	−77.53	0.31	88.97	0.34	−77.42	0.41	89.54	0.53
2019-07-14	−77.68	0.30	88.31	0.36	−78.25	0.39	88.29	0.43
2019-07-14	−77.32	0.36	88.54	0.36	−78.32	0.46	90.41	0.37
2019-07-18	−0.11	0.11	9.59	0.44	−1.35	0.23	6.60	0.47
2019-07-18	−0.10	0.09	9.62	0.44	−2.55	1.02	7.49	0.78
2019-07-18	−0.12	0.11	9.80	0.47	−2.18	1.06	7.49	0.63
2019-07-20	−2.67	1.05	13.93	0.87	−5.15	0.46	10.36	0.59
2020-02-27	−1.08	0.66	9.85	1.15	−2.15	1.33	9.39	1.50
2020-02-27	−0.41	0.41	11.11	0.77	−2.48	0.85	8.36	0.32
2020-02-28	0.00	0.00	9.56	0.11	−1.30	0.65	8.66	0.55
2020-02-28	−0.01	0.01	9.56	0.12	−0.95	0.59	8.43	0.47
2020-02-29	−2.15	1.28	10.58	1.13	−4.34	0.70	9.45	0.33
2020-02-29	−2.61	1.31	10.86	1.13	−5.53	2.33	9.14	1.48
2020-03-01	−4.56	0.31	17.13	0.28	−4.64	0.36	16.82	0.34
2020-03-01	−4.30	0.35	17.21	0.31	−3.74	0.57	17.61	0.47
2020-03-01	−4.59	0.26	17.66	0.21	−5.38	0.33	16.78	0.31
2020-03-01	−4.88	0.27	17.73	0.22	−5.51	0.27	17.43	0.28
2020-03-12	−14.69	0.15	26.63	0.16	−14.88	0.20	26.03	0.18
2020-03-12	−14.54	0.14	26.88	0.14	−14.01	0.19	26.69	0.17

Table 7: Extracted mean radial velocity measurements and their standard deviations, obtained from posterior distributions of fit Voigt profiles for the absorption features at 6067.161 Å and 6548.047 Å.

Date	Hα at 6564.614 Å				Fe I Line at 6679.828 Å			
	v_0 [km/s]		v_1 [km/s]		v_0 [km/s]		v_1 [km/s]	
	Mean	Std	Mean	Std	Mean	Std	Mean	Std
2019-02-04	−64.45	0.16	76.23	0.17	−63.23	0.18	75.16	0.21
2019-02-13	−13.02	0.55	16.28	0.29	−11.66	0.31	24.04	0.27
2019-02-13	−12.72	0.80	16.00	0.35	−11.45	0.26	23.78	0.23
2019-02-18	−20.42	0.98	21.65	0.51	−15.16	0.13	27.29	0.12
2019-02-18	−18.85	1.77	23.19	0.99	−15.04	0.13	26.50	0.12
2019-04-29	−23.58	0.81	19.90	0.13	−12.49	0.14	24.77	0.12
2019-04-29	−23.64	0.83	19.89	0.17	−12.85	0.14	24.77	0.13
2019-04-30	−19.89	0.54	17.83	0.19	−11.40	0.13	23.47	0.12
2019-04-30	−20.05	0.57	17.90	0.23	−11.52	0.13	23.77	0.12
2019-05-11	−73.39	0.21	86.40	0.22	−73.04	0.23	83.51	0.26
2019-05-11	−72.23	0.17	85.42	0.18	−71.73	0.18	83.10	0.22
2019-05-12	−46.94	0.18	58.51	0.18	−41.47	0.18	52.86	0.19
2019-05-23	−19.83	0.18	24.89	0.28	−14.13	0.20	26.34	0.18
2019-07-04	−12.28	4.08	19.10	3.32	−10.06	0.30	22.60	0.26
2019-07-13	−71.19	0.34	84.33	0.40	−69.45	0.38	80.83	0.38
2019-07-13	−70.98	0.44	84.31	0.47	−70.33	0.44	81.65	0.61
2019-07-13	−71.05	0.36	84.96	0.41	−70.65	0.38	81.27	0.44
2019-07-14	−78.66	0.36	92.94	0.39	−78.91	0.44	89.79	0.47
2019-07-14	−78.22	0.46	92.04	0.46	−77.14	0.52	88.33	0.52
2019-07-14	−77.43	0.35	91.99	0.37	−78.00	0.34	88.56	0.39
2019-07-14	−78.05	0.33	91.72	0.33	−78.23	0.32	88.52	0.31
2019-07-14	−78.27	0.32	91.76	0.32	−77.96	0.35	89.19	0.33
2019-07-14	−78.03	0.33	90.84	0.35	−77.28	0.32	88.75	0.37
2019-07-18	−3.68	0.40	18.11	0.40	−0.31	0.24	8.84	0.58
2019-07-18	−5.90	0.59	16.70	0.56	−0.53	0.48	8.12	0.84
2019-07-18	−4.02	0.61	17.20	0.55	−1.38	1.12	7.99	0.90
2019-07-20	−1.09	0.52	15.35	1.20	−2.46	1.19	14.01	0.95
2020-02-27	−4.49	2.61	14.76	3.31	−0.92	0.67	10.13	1.23
2020-02-27	−4.44	0.43	18.48	0.42	−2.22	1.64	10.19	2.10
2020-02-28	−4.43	2.56	15.26	4.07	−0.03	0.03	9.19	0.14
2020-02-28	−4.66	2.69	15.08	3.92	−0.04	0.04	8.72	0.20
2020-02-29	−4.85	0.71	16.84	0.75	−2.71	1.96	10.26	1.43
2020-02-29	−6.30	0.41	15.69	0.43	−4.91	0.38	8.90	0.50
2020-03-01	−1.87	2.58	12.77	3.76	−4.28	0.35	17.28	0.32
2020-03-01	−0.32	0.43	9.88	0.30	−4.11	0.42	17.73	0.36
2020-03-01	−0.86	0.93	10.19	0.51	−5.37	0.35	17.54	0.31
2020-03-01	−0.44	0.46	9.95	0.35	−4.65	0.31	18.09	0.28
2020-03-12	−12.19	0.74	18.18	0.64	−14.57	0.16	26.46	0.15
2020-03-12	−8.24	1.20	22.96	1.66	−14.82	0.16	26.92	0.15

Table 8: Extracted mean radial velocity measurements and their standard deviations, obtained from posterior distributions of fit Voigt profiles for the absorption features at 6564.614 Å and 6679.828 Å.

6.2 Line Depth Stellar Classification

For the stellar classification, it was decided to denote the star with the deeper feature as 'star 1', and the star with the less deep feature as 'star 2'. Subsequently, the line depths of the lines selected in Table 2 were analysed in hopes of classifying the stars based on this criterion. It was observed that the Hα, possibly due to its broad and deep nature, looked identical and could not be used to distinguish between the stars. Thus, it was the remaining lines that were investigated. In the figures below are presented the Voigt fits over the observed spectra for different epochs and the attempts to classify the stars using the FeI line at 5885.447 Å.

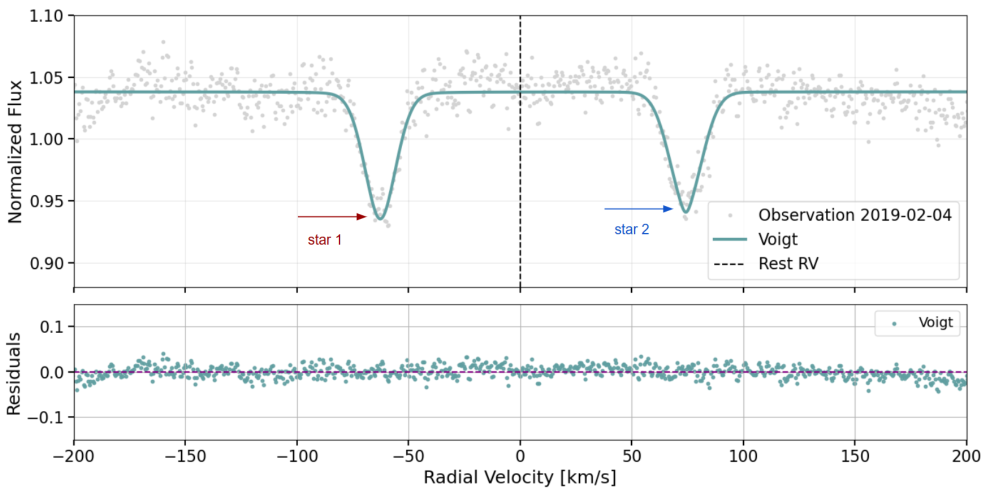

Figure 15: Plot of the Voigt best fit and the observed spectrum for the FeI line at 5885.447 Å, epoch 2019-02-04. With arrows are indicated the attempted classification. The residuals of the Voigt fit are plotted below.

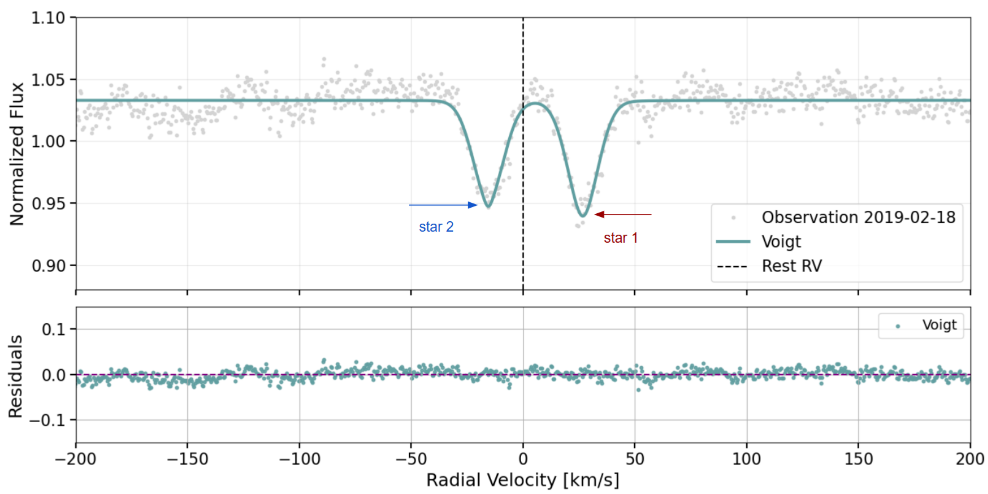

Figure 16: Plot of the Voigt best fit and the observed spectrum for the FeI line at 5885.447 Å, epoch 2019-02-18. With arrows are indicated the attempted classification. The residuals of the Voigt fit are plotted below.

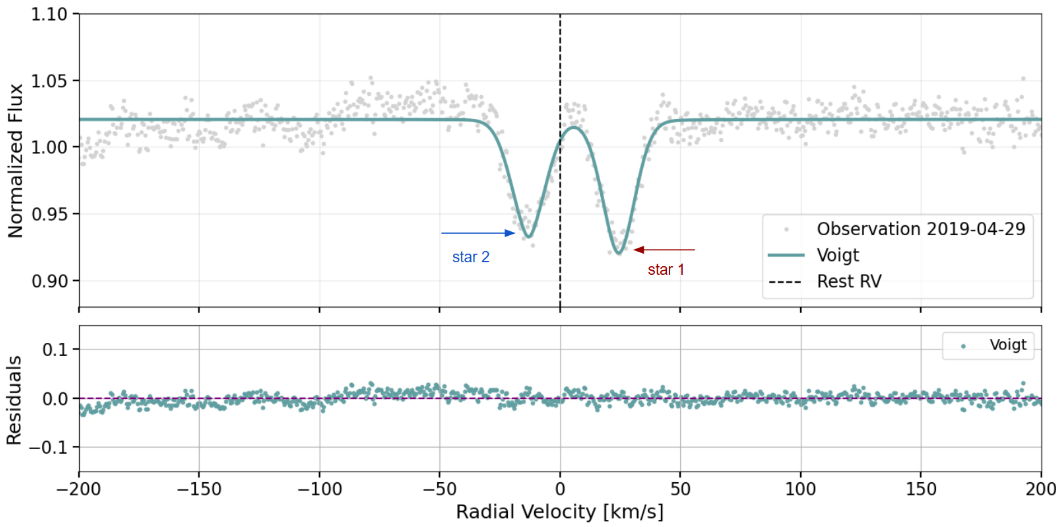

Figure 17: Plot of the Voigt best fit and the observed spectrum for the FeI line at 5885.447 Å, epoch 2019-04-29. With arrows are indicated the attempted classification. The residuals of the Voigt fit are plotted below.

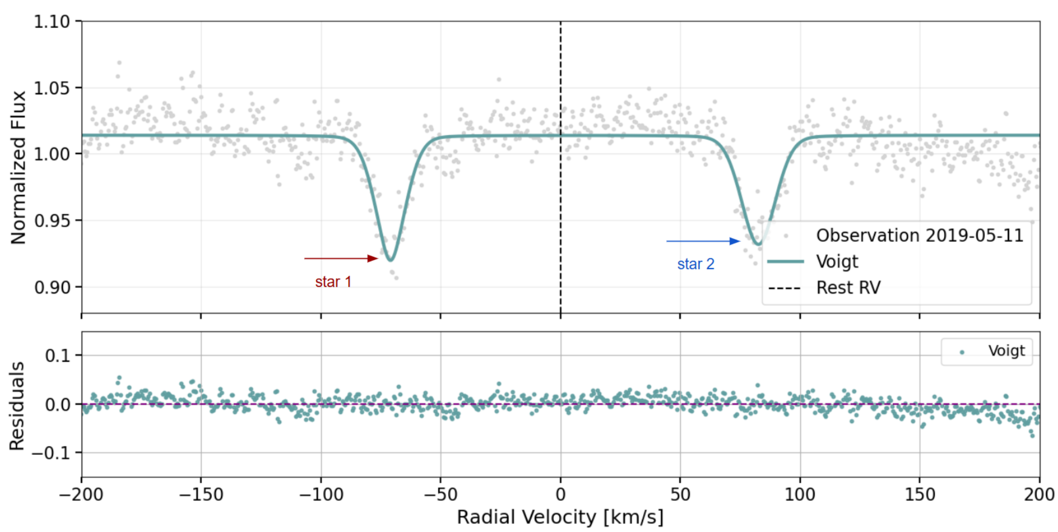

Figure 18: Plot of the Voigt best fit and the observed spectrum for the FeI line at 5885.447 Å, epoch 2019-05-11. With arrows are indicated the attempted classification. The residuals of the Voigt fit are plotted below.

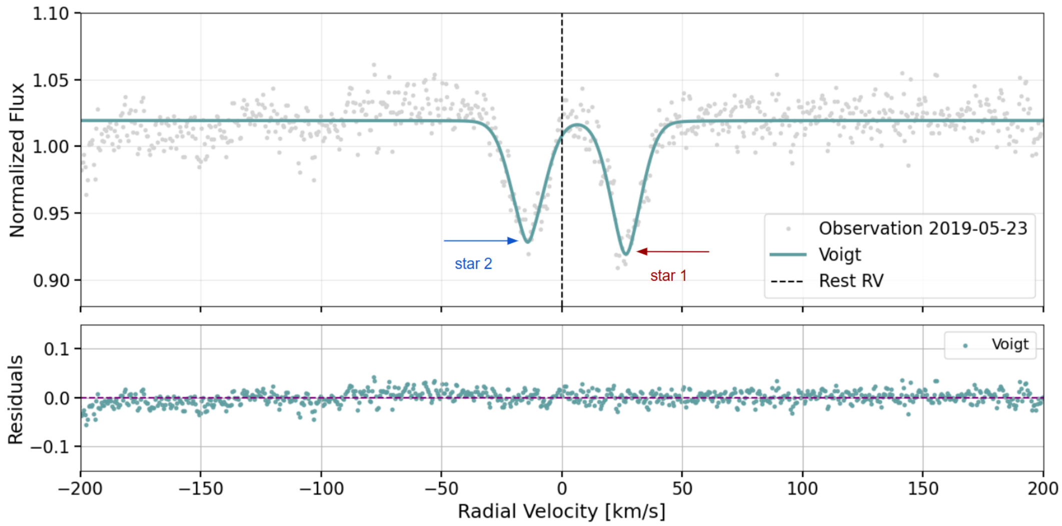

Figure 19: Plot of the Voigt best fit and the observed spectrum for the FeI line at 5885.447 Å, epoch 2019-05-23. With arrows are indicated the attempted classification. The residuals of the Voigt fit are plotted below.

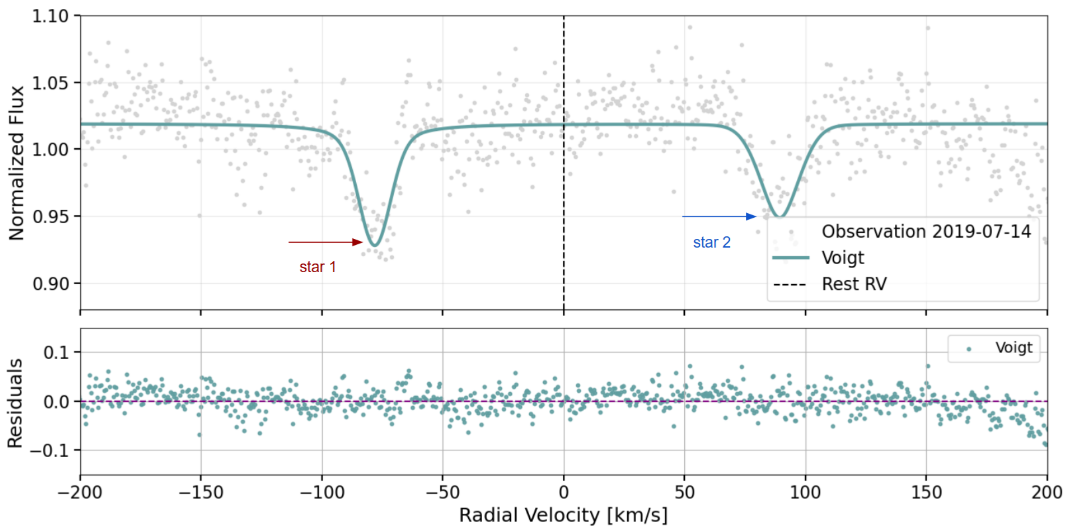

Figure 20: Plot of the Voigt best fit and the observed spectrum for the FeI line at 5885.447 Å, epoch 2019-07-14. With arrows are indicated the attempted classification. The residuals of the Voigt fit are plotted below.

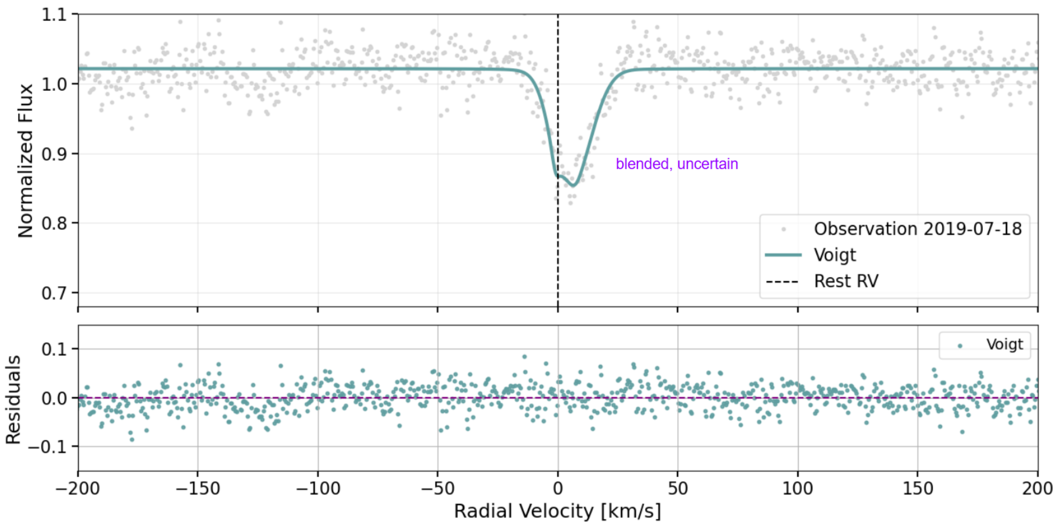

Figure 21: Plot of the Voigt best fit and the observed spectrum for the FeI line at 5885.447 Å, epoch 2019-07-18. Note that the line blending prevents the accurate classification. The residuals of the Voigt fit are plotted below.

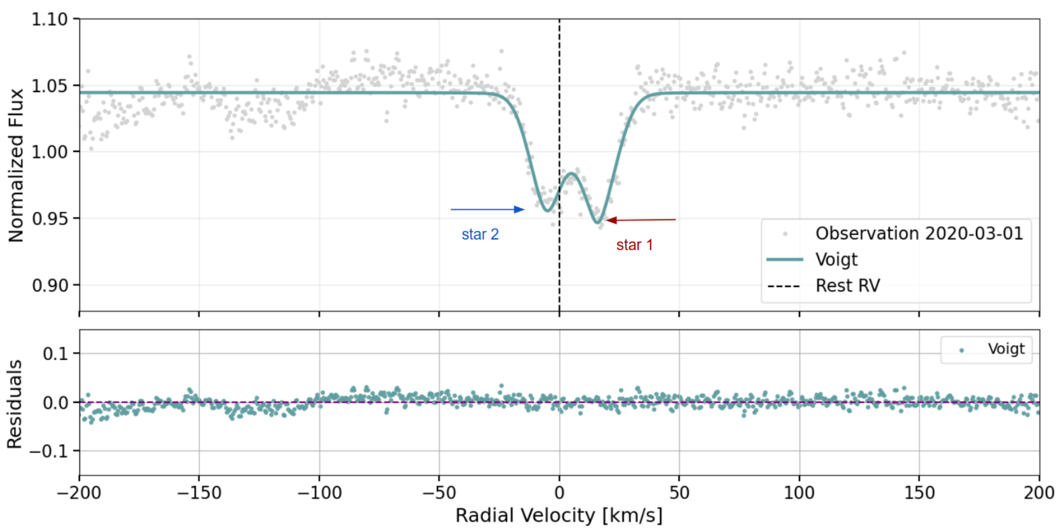

Figure 22: Plot of the Voigt best fit and the observed spectrum for the FeI line at 5885.447 Å, epoch 2020-03-01. With arrows are indicated the attempted classification. The residuals of the Voigt fit are plotted below.

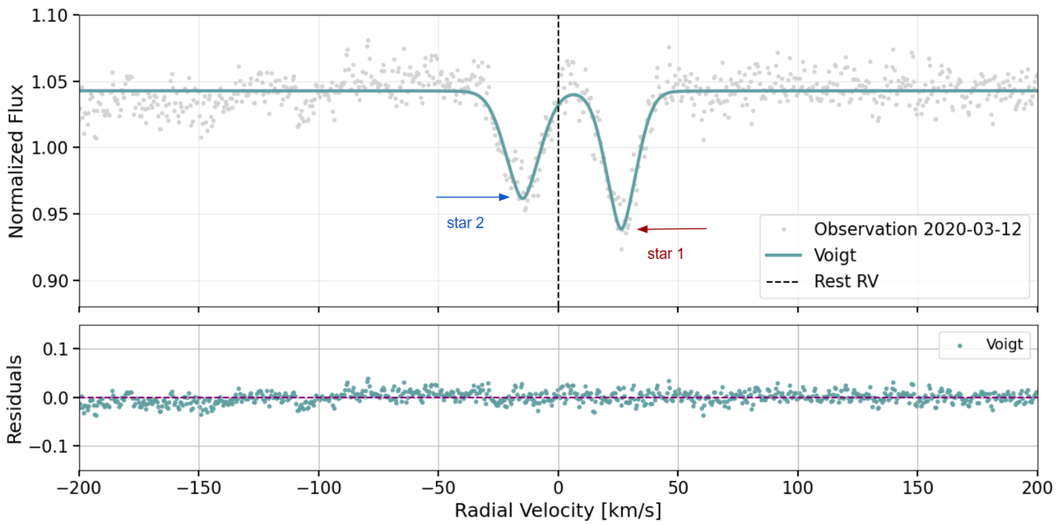

Figure 23: Plot of the Voigt best fit and the observed spectrum for the FeI line at 5885.447 Å, epoch 2020-03-12. With arrows are indicated the attempted classification. The residuals of the Voigt fit are plotted below.

It was attempted then to compare the classification resulting from one such analysis with other lines, and to confirm the classification or help render a result in the case of uncertainty. In some cases such comparisons resolved the uncertainty, while in others they persisted. A more systematic selection of more temperature-sensitive lines could perhaps serve for a more definitive classification.

6.3 Zoomed pySME Fit Results

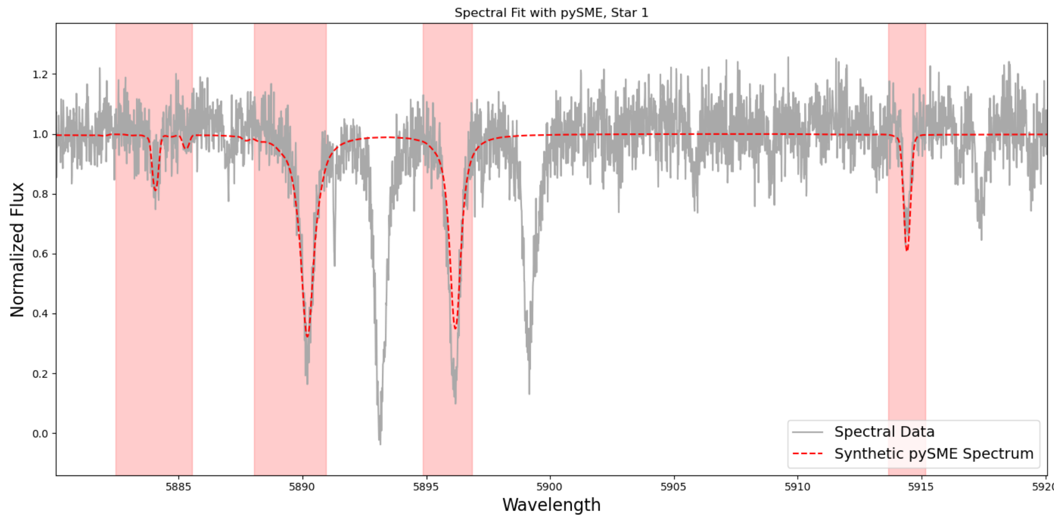

Figure 24: Synthetic spectrum resulting from the SME solver for the dataset corresponding to star 1 for the epoch 2019-07-13. In gray dots is represented the observed flux used as the data. In shaded regions are the segments included in the fit. The wavelength is given in [Å]. This is a zoomed in version around the NaI D line.

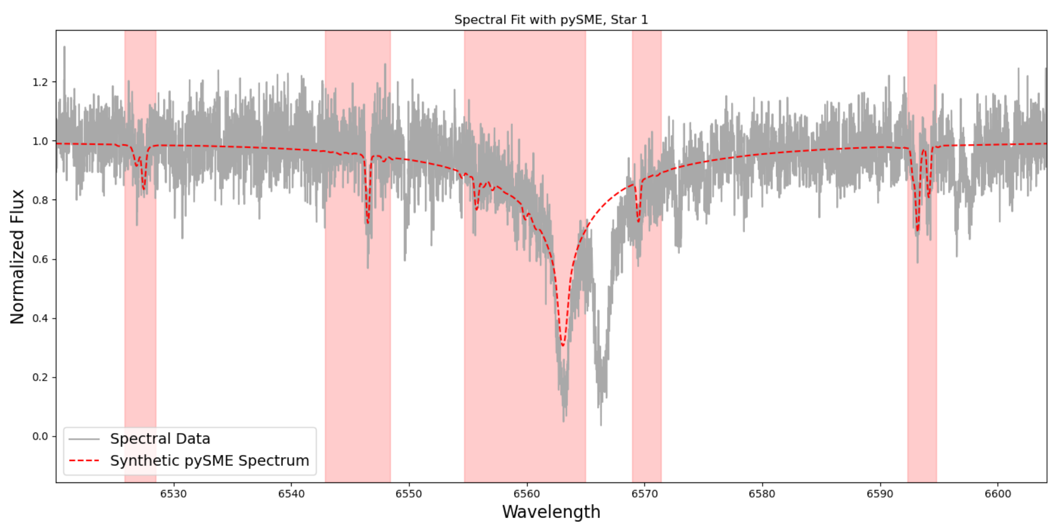

Figure 25: Synthetic spectrum resulting from the SME solver for the dataset corresponding to star 1 for the epoch 2019-07-13. In gray dots is represented the observed flux used as the data. In shaded regions are the segments included in the fit. The wavelength is given in [Å]. This is a zoomed in version around the Hα line.

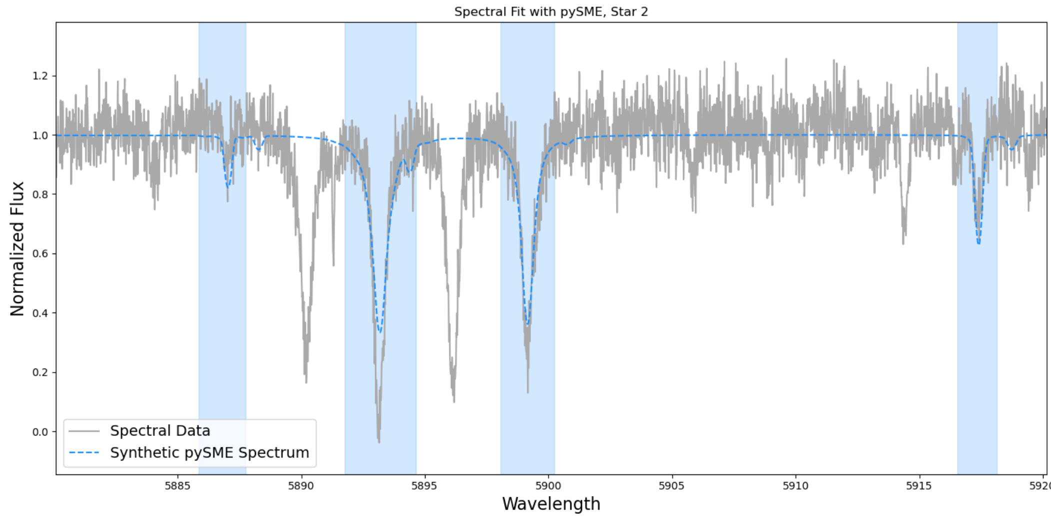

Figure 26: Synthetic spectrum resulting from the SME solver for the dataset corresponding to star 2 for the epoch 2019-07-13. In gray dots is represented the observed flux used as the data. In shaded regions are the segments included in the fit. The wavelength is given in [Å]. This is a zoomed in version around the NaI D line.

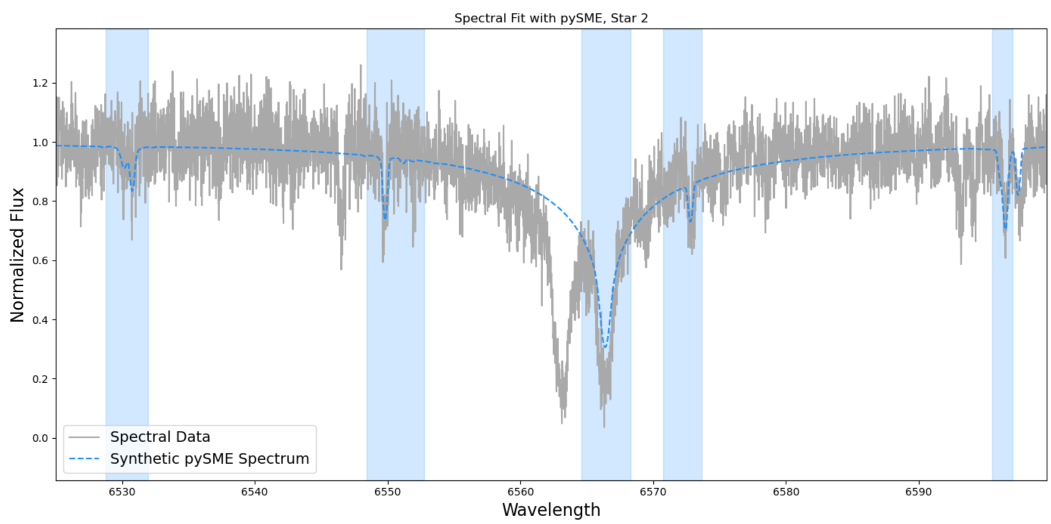

Figure 27: Synthetic spectrum resulting from the SME solver for the dataset corresponding to star 2 for the epoch 2019-07-13. In gray dots is represented the observed flux used as the data. In shaded regions are the segments included in the fit. The wavelength is given in [Å]. This is a zoomed in version around the Hα line.